

AD-A123 062

OBSERVATIONS ON BUBBLE DYNAMICS AT HIGH PRESSURES AND
BUBBLE DYNAMICS IN STAGNATION FLOW(U) CALIFORNIA UNIV
SAN DIEGO LA JOLLA A T ELLIS ET AL. 30 NOV 82

1/1

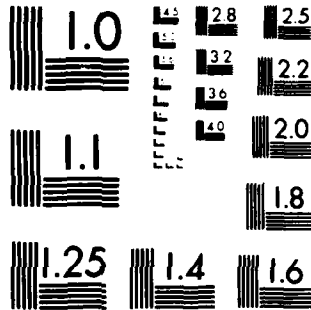
UNCLASSIFIED

N00014-79-C-0547

F/G 20/4

NL

END
DATE
FILMED
DTIC



MICROCOPY RESOLUTION TEST CHART
NATIONAL BUREAU OF STANDARDS-1963-A

AD A 123062

DTIC FILE COPY

SECURITY CLASSIFICATION OF THIS PAGE (When Data Entered)

REPORT DOCUMENTATION PAGE		READ INSTRUCTIONS BEFORE COMPLETING FORM
1. REPORT NUMBER FINAL REPORT	2. GOVT ACCESSION NO. AD-A123062	3. RECIPIENT'S CATALOG NUMBER
4. TITLE (and Subtitle) Observations on Bubble Dynamics at High Pressures and Bubble Dynamics in Stagnation Flow	5. TYPE OF REPORT & PERIOD COVERED Final Report 09-01-79 to 09-30-81	
7. AUTHOR(s) Albert T. Ellis John E. Starrett	6. PERFORMING ORG. REPORT NUMBER	
9. PERFORMING ORGANIZATION NAME AND ADDRESS University of California, San Diego La Jolla, California 92093	8. CONTRACT OR GRANT NUMBER(s) N00014-79-C-0547	
11. CONTROLLING OFFICE NAME AND ADDRESS Office of Naval Research, Code 438 Fluid Mechanics Program Arlington, Virginia 22217	10. PROGRAM ELEMENT, PROJECT, TASK AREA & WORK UNIT NUMBERS	
14. MONITORING AGENCY NAME & ADDRESS (if different from Controlling Office)	12. REPORT DATE 11-30-82	
	13. NUMBER OF PAGES	
	15. SECURITY CLASS. (of this report) Unclassified	
16. DISTRIBUTION STATEMENT (of this Report) Per distribution list for unclassified technical reports and reprints issued under contract N00014-79-C-0547 Task Nr 062-283		
<div style="border: 1px solid black; padding: 5px; text-align: center;"> DISTRIBUTION STATEMENT A Approved for public release; Distribution Unlimited </div>		
17. DISTRIBUTION STATEMENT (of the abstract entered in Distribution Statement A)		
18. SUPPLEMENTARY NOTES		
19. KEY WORDS (Continue on reverse side if necessary and identify by block number) Cavitation, High Speed Photography, Ruby Laser		
20. ABSTRACT (Continue on reverse side if necessary and identify by block number) Experimental and theoretical research on bubble collapse at high ambient pressure and in stagnation flow near a rigid boundary.		

DTIC
SELECTED
JAN 4 1983
H

DD FORM 1 JAN 73 1473

EDITION OF 1 NOV 68 IS OBSOLETE
S. N. 0102- LF-014-5601

SECURITY CLASSIFICATION OF THIS PAGE (When Data Entered)

82 12 09 002



Proceedings of the Fifth International Conference
on
Erosion by Liquid and Solid Impact

Newnham College
Cambridge
UK

3-6 September 1979

Published by Cavendish Laboratory, University of Cambridge
Printed by the Royal Aircraft Establishment, Farnborough, Hants
Crown Copyright ©

PREFACE

This is the fifth Conference in a series in which three have been held at Meersburg, in the Federal German Republic (1965, 1967 and 1974) and one at Elvehøi in Hampshire, U.K. (1970). These earlier conferences were sponsored by Dornier System GmbH acting on behalf of the Federal German Ministry of Defence and by the U.K. Ministry of Defence (Procurement Executive). The Materials Department of the Royal Aircraft Establishment, Farnborough, co-ordinated the U.K. effort and undertook the production of the Proceedings: Andrew Fyall and Roy King were Editors. Not all the Conferences in this series have had the same title. Early ones were predominantly about liquid impact and rain erosion, but inevitably the scope extended to include "associated phenomena". In this Meeting it was decided to give approximately equal time to the major topics of liquid impact, solid impact and cavitation erosion.

The response to the "call for papers" was extremely encouraging. Over 100 synopses were submitted, and of these 80 were highly recommended by the Referees; the remainder frequently contained excellent material but were thought to be peripheral to the main themes of the Conference. With so many good papers the Conference Committee decided to expand what was planned to be a three day Meeting into a four day one. The final programme is likely to have about 75 papers, and the Committee are delighted that almost every group actively engaged in erosion research is likely to be represented.

The Committee felt strongly that every effort should be made to have the Proceedings available at the time of the Conference. This meant asking for "camera-ready" papers. We are most grateful to the Authors for preparing their papers in this way and keeping to suggested deadlines. At the time of writing, it looks as if all but a very few will be included in the Proceedings. Since this volume will be an important and up-to-date record of erosion research, extra copies are being prepared. It will, therefore, be possible for individuals and libraries to purchase further copies.

The Authors have been allocated lecture times of 10, 15 or 20 minutes. The Committee have emphasised to Authors that this does not reflect their opinions of the likely quality of the paper, but are simply times expected for adequate delivery of the subject matter. Authors have been given the opportunity to ask for an increased time allowance. What this means is that the times allowed in the final programme have been agreed by the Authors. Session Chairmen we feel will be reinforced by this and will act firmly and fairly to ensure the successful running of the Conference.

We are grateful to Professor David Tabor for acting as Conference Chairman. His now classic work with the late Professor Bowden, on Friction and Lubrication involved pioneer work on contact stress, hardness, elastic deformation and surfaces; all are major themes in the present Conference. The Committee would like to express their appreciation to the International Advisors for their help in publicising the Meeting and for their valuable advice at all stages of the planning of the Conference. I would like to thank the Organising Committee for their hard work and support. Dr. Norman Corney and Dr. John Lancaster of Farnborough, together with Mr. Peter Rolls and Mr. Peter Pinnock of the printing department at Farnborough, took the full load of converting the "camera-ready" papers into the Proceedings. All delegates, and in fact all readers of the Proceedings, will feel grateful for their efforts. The Cambridge members of the Committee have shared all the local organisational work. I would like to add particular thanks to my two colleagues in the Cavendish, Dr. David Gorham and Dr. John Matthewson (the most "local" of all the Committee members) and consequently the first in line for urgent jobs. They have "battled" with local printers, checked lists, sealed envelopes etc. with alacrity and enthusiasm. No organisational work can proceed satisfactorily without devoted secretarial help, and the noble ladies in the case of this Conference are Mrs. Felicity (Flick) Ellis and Mrs. Gerie Lonzarich.

The sponsors for this Meeting are the United States Army and Air Force, through the U.S. Procurement Agency, Europe, the United States Navy through their European Office and the Ministry of Defence (Procurement Executive) U.K. The Royal Aircraft Establishment, U.K. took full responsibility for preparing the Conference Proceedings. All these sponsors are thanked for their generosity.

DR. JOHN FIELD

Accession for	
NTIS GRA&I	
DTIC TAB	
Unannounced	
Justification	
By file	
Distribution	
Availability Codes	
Dist	Avail and/or Special
A	



CONFERENCE CHAIRMAN

Professor D. Tabor, F.R.S.

Cavendish Laboratory,
Department of Physics,
University of Cambridge, U.K.

ORGANISING COMMITTEE

Dr. J.E. Field (Secretary)

Dr. D.A. Gorham

Dr. M.J. Matthewson

Dr. J.H. Brunton

Dr. I.M. Hutchings

Dr. N.S. Corney

Dr. J.K. Lancaster

Cavendish Laboratory,
Department of Physics,
University of Cambridge, U.K.

Department of Engineering,
University of Cambridge, U.K.

Department of Metallurgy and
Materials Science, University of
Cambridge, U.K.

Ministry of Defence (Procurement
Executive), Farnborough, U.K.

Royal Aircraft Establishment,
Farnborough, U.K.

INTERNATIONAL ADVISORS

Dr. W.F. Adler

Prof. I. Finnie

Dr. G. Hoff

Prof. M.B. Lesser

Dr. C.M. Preece

G.F. Schmitt, Jr.

E.T.I., California, U.S.A.

University of California, U.S.A.

Dornier, Federal German Republic.

University of Luleå, Sweden.

Bell Labs., New Jersey, U.S.A.

United States Air Force, Ohio, U.S.A.

Fifth International Conference on Erosion by
Liquid and Solid Impact, (ELSI V),
Dr. J.E. Field (Secretary of Organising Committee),
Cavendish Laboratory,
Madingley Road,
Cambridge CB3 0HE,
U.K.

Proc. 5th Int. Conf. on Erosion by Solid and Liquid Impact

OBSERVATIONS ON BUBBLE DYNAMICS IN JET FLOWS AND AT HIGH AMBIENT PRESSURES

A.T. Ellis and J.E. Starratt
University of California, San Diego

Recent development by the authors of a unique ruby laser light source has permitted moving pictures of bubble growth and collapse to be made during a two-millisecond observation time at rates from 100,000 to 1,000,000 frames per second with exposure time of approximately 2×10^{-6} seconds.

The coherent nature of the laser illumination revealed shock waves without need for Schlieren techniques. It seemed quite evident that bubble collapse microjets rather than shockwaves caused greater damage to fused quartz specimens. There also seemed to be damaging jets generated during bubble rebound.

Since possible use of cavitation to assist deep bore earth drilling has been proposed, experiments were conducted utilizing spark generated cavities in water and non-Newtonian solutions at ambient pressures up to 35 MPa (10,000 ft bore-hole depth). Radius-time curves showed fairly good agreement with the classical theory of Lord Rayleigh even above the 22 MPa critical point for water. Flow generated cavitation in jets from types of nozzles including that of Leach and Walker were observed.

To facilitate analysis, single bubbles were generated in a flow normally impacting a solid wall. The bubbles assumed an elliptical shape near the stagnation region and relatively fine bubble jets were observed during both collapse and rebound. These observations appear to qualitatively support earlier theoretical work by many investigators including Naude and Ellis [1], Benjamin and Ellis [2], F.P. Bowden [3], Plesset and Chapman [4] and more recently, Voinov and Voinov [5].

Research supported by Office of Naval Research & National Science Foundation.

HISTORICAL BACKGROUND AND INTRODUCTION

Effects of two basic phenomena have been observed at least as long as the eighteenth century. Theoretical treatment of cavitation probably began in 1754 with Euler [6], and the use of a hollow explosive charge to form a jet was mentioned in 1792. Theoretical work on the explosive "Munroe" jets dates from the World War II work of Sir Geoffrey Taylor [7], and others [8].

Although cavitation was easily observed long ago, the actual mechanics of bubble collapse was not, due to the high velocities involved. Theoretical work by Rayleigh [9], and others [10], even as late as the 1960's was consequently preoccupied with spherically symmetric bubble collapse and damage-causing mechanism, but it has become increasingly apparent to many investigators that jets formed during cavitation bubble collapse are probably even more damaging. The close connection, therefore, between cavitation damage and "Munroe" jets was relatively late in being realized. A more detailed survey of the work leading to this is made in the paper "On Jets and Shockwaves from Cavitation," by A.T. Ellis in the Proceedings of the 6th Symposium on Naval Hydrodynamics, held in Washington, D.C. in 1966. Briefly, it appears that the cavitation jet was suspected as early as 1944 [11], but actual high-speed photographic proof was not available until 1958 when Naudé and Ellis using a Kerr cell camera developed by Ellis in 1952 [12], took 200,000 frames per second, 0.1

microsecond exposure pictures of the actual collapse on photoelastically sensitive solids [13]. A second-order perturbation theory was developed by them at the same time which extended the original first-order theory of Plesset and Mitchell published in 1956 [14]. Much later work confirming these results and extending them has been done by others.

This work, however, was motivated generally by the need to suppress cavitation damage and was not directed toward its use for drilling or excavation. This idea seems to have originated with various Russian workers but in recent years it has received so much popularity that the literature is too large to be properly referenced.

Three main sources of literature on this subject come from meetings of the Royal Society of London in 1965, and the British Hydrodynamics Research Association in 1972 and again in 1974. In particular, the papers of Virgil Johnson and his associates at the latter two meetings [15], [16] are of particular interest for the drilling problem. In their papers, they describe operation of their "cavijet" which indeed is impressive for surface drilling or mining.

It is felt that the implications of the theory presented by Benjamin and Ellis [17] at the Royal Society of London in 1965 form a basis for the explanation of the effectiveness of the "cavijet". The basic point is that rapid deformation of the cavity leads, by

momentum considerations, to self-propel the centroid in the axial, or mean flow direction. There is thus an additional effect concentrating energy into the jet which is highly dependent on the centroid velocity. The practical significance is that bubbles collapsing in a high-speed flow relative to the surface they will eventually impact should be much more damaging than if they were collapsing in a stationary medium. Perhaps the first observation of this was the paper by Knapp [18] in 1955 in which small cavitation bubbles were carried along the boundary of a larger "supercavitating" stationary cavity and into the stagnation region where their unusually high translational velocity created conditions for heavy damage proportional to the fifth or sixth power of the velocity. Significantly, however, Knapp estimated that the fraction of bubbles which were effective in causing damage was very small. This means that the location and size of the bubble relative to the surface to be damaged is very critical.

The proposed means of overcoming these difficulties was to provide a system wherein a spark-generated bubble was formed in an already existing flow of as high a velocity as possible. The generation point would not be immediate to the solid face to be drilled, but would be the proper distance away such that the bubble would grow and start to collapse as it is swept toward it. When it reached the proper standoff distance, another spark generated bubble would be initiated upstream and a strong shock wave caused by this spark. This shock wave would propagate downstream to encounter the upper surface of the previously generated bubble and initiate a jet in the direction of propagation of the shock. This experiment was performed by Ellis and his graduate student, Paul Gruber, at Caltech in 1967 [19]. However, the shock wave was generated by a spark in a tube over a rising curved air-water interface and the pressures used and velocities attained were low. The results showed a factor of approximately 3 for the ratio of jet velocity to main flow velocity, and this agreed with the observations of Bowden wherein microjet velocities of 1900 meters per second for main jet velocities of 650 meters per second were observed [3].

SPHERICAL BUBBLE DYNAMICS IN A NON-NEWTONIAN LIQUID

The theory of spherical bubble growth and collapse in an incompressible liquid was published by Lord Rayleigh in 1917.

If we include stresses due to surface tension, σ , Newtonian viscosity, μ_0 , and non-Newtonian fluid stresses based on the two parameter Oldroyd model [20] then the bubble equation developed by Ellis and Ting [21] becomes

$$\rho(R\ddot{R} + \frac{3}{2}\dot{R}^2) + \frac{2\sigma}{R} + 4\mu_0\frac{\dot{R}}{R} + \frac{2\mu_0 C[\eta]}{\lambda} \int_0^{\frac{t-\tau}{\lambda}} \frac{e^{-\tau/\lambda}}{\lambda} \frac{\dot{R}(\tau)}{R(\tau)} \left[1 + \frac{R^3(\tau)}{R^3(t)} \right] d\tau + P_\infty - P_b = 0 \quad (1)$$

where P_∞ is the ambient pressure far from the bubble and P_b is the pressure inside the bubble. $[\eta]$ is the intrinsic viscosity, C the concentration, and λ the "terminal relaxation time" [20] of dilute polymer solutions. It may be noticed that the integral representing non-Newtonian effects is of the "memory" type where the stress depends on the history of the strain and strain rate as well as its current value. In addition a term representing the effect of non-condensable gas in the bubble may be included as is done later in this section. If terms involving viscosity are neglected, the equation becomes the familiar Rayleigh equation.

Fortunately, from the standpoint of data reduction and calculations in the present work, only the inertial stress and the pressure were judged to be significant. This was based on the numerical values of the parameters in the experiment. It is helpful to put equation (1) in non-dimensional terms to see this. The following quantities are therefore introduced [22]:

$$\hat{R} = \frac{R}{R_0} \quad \hat{t} = \frac{t}{\tau} \quad \hat{\tau} = \frac{\tau}{\tau} \quad \text{where } \tau = .915R_0 \sqrt{\frac{\rho}{\Delta P}}$$

$$\text{Reynolds number, } R_e = \frac{\rho R_0^2}{\mu_0 \tau}$$

$$\text{Webers number, } N_w = \frac{\rho R_0^3}{2\sigma \tau^2}$$

$$\text{Deborah number, } N_D = \frac{\lambda}{\tau} \text{ and } \hat{\tau} \text{ indicates } \frac{d}{d\hat{\tau}}.$$

Equation (5) then becomes:

$$\hat{R}\hat{R}'' + \frac{3}{2}\hat{R}'^2 + \frac{4}{R_e} \frac{\hat{R}'}{\hat{R}} + \frac{1}{N_w \hat{R}} + \frac{2C[\eta]}{N_D \hat{R}} \int_0^{\hat{t}-\hat{\tau}} \frac{e^{-\hat{\tau}}}{\hat{\tau}} \frac{\hat{R}'(\hat{\tau})}{\hat{R}(\hat{\tau})} \left[1 + \frac{\hat{R}^3(\hat{\tau})}{\hat{R}^3(\hat{t})} \right] d\hat{\tau} = -1 \quad (2)$$

where the positive and negative signs on the term on the right side of the equation are for the growth and collapse cases, respectively.

Typical values for the experiments reported here are:

$$\text{Reynolds number, } R_e = 60,000 \text{ to } 74,000 \\ \text{Deborah number, } N_D = 20 \text{ to } 80.$$

The denominator of the coefficient of the integral is thus in the range 1.2×10^6 to 6.2×10^6 . Experimental data on the value of the intrinsic viscosity, $[\eta]$, at our extremely high strain rates ($\approx 3 \times 10^7$) is unavailable, but a theoretical treatment by Lumley [23] indicates it may be very high. Because of this we did some experiments with polyethylene oxide at up to 300 parts per million by weight concentration. No measurable difference could be noticed and we therefore concluded that neglecting it theoretically was justified. At our Reynolds numbers it was even more obvious that the ordinary Newtonian viscosity would

have a negligible effect. This is an important simplifying assumption since it means that bubble dynamics will not be affected at high ambient pressures by the viscometric properties of the drilling mud.

The effects of compressibility of the liquid are also neglected as far as bubble dynamics are concerned since maximum observed bubble wall velocities were only about one-fifth sound speed in the liquid.

Measured shock wave velocities were approximately 1.63×10^3 cm/sec compared to a sound speed of 1.49×10^3 cm/sec at a radius of 0.5 cm. An estimate of shock pressure at this radius is 670 MPa (97,000 PSI). This is in good agreement with measurements made by Sandia Corporation but is nearly an order of magnitude lower than stresses developed by the cavitation jet.

The experimentally observed bubbles collapse to a finite volume (typically 6% of maximum volume) and rebound indicating the presence of non-condensable gas in the bubble. Rayleigh showed that, if z_{min} is the minimum volume ratio of the bubble (R/R_0), then:

$$\left[RR + \frac{3}{2} R^2 \right] = -P_\infty \left[1 + \frac{R_0^3}{R^3} \left(\frac{1 - z_{min}}{2n z_{min}} \right) \right] \quad (3)$$

Equation (3) was solved numerically by a fourth order Runge-Kutta technique. The resulting normalized curves of R vs. t are shown in Figures 1 and 2. Figure 1 is the theoretical Rayleigh curve with $z_{min}=0$ for both growth and collapse. Figure 2 shows the curves of Radius (R) and velocity (\dot{R}) and acceleration (\ddot{R}) for collapse of bubbles by both the vapor model (R_0) and the gas filled model (R_G) of equation (3). In this solution the minimum volume of the bubble was chosen as $.064 V_0$ to be representative of the experimental data. As the minimum volume is allowed to go to 0 the curve R_G approaches the curve R_0 , but a gas-filled model will always show a sharp acceleration spike at minimum volume when the bubble rebounds and is thus a fundamentally different solution than the vapor model.

It should be remembered, however, that solid wall proximity will cause a jet to form and cause damage before minimum volume is reached so that gas content may not be a large factor in that case. The experimental bubbles at high ambient pressure reported here were not near a wall and were not observed to form jets.

OBSERVATION OF SPARK GENERATED CAVITIES AT HIGH PRESSURES

The high speed laser camera was used to obtain photographic histories of bubble radii in several liquids at ambient pressures from 1,000 to 5,000 psi (6.89 to 34.5 MPa). Spark generated bubbles were created in a high pressure experimental chamber designed and built by Sandia Corporation, which was placed between the pulse locked laser and the camera lens. The chamber is cylindrical, with sapphire optical windows concentrically mounted at each end and a high voltage feed through

that enters the cylinder radially at its midpoint. The feed through was modified to hold a spark electrode fabricated from standard 1/16" diameter thoriated tungsten welding electrode stock, tapered to a point. The grounded electrode is identical and is mounted directly to the inside wall of the cylinder at 90° to the high voltage electrode, forming a spark gap on the cylinder/optical axis. Photographs of the experimental set up are shown in Figure 3 and Figure 4.

The sparks were made by discharging a 1.93 ufd capacitor through the spark gap with a 7390 hydrogen thyratron. The capacitor was initially charged to 13 KV. Typical voltage and current waveforms of the discharge pulse at the spark gap observed with different capacitors charged to voltages from 5 to 15 KV indicate a predictable D.C. gap resistance of about 0.10 ohms, with a current waveform that is closely sinusoidal of one-half cycle and width of about 5 μ s. Thus the energy in the spark can be determined by measuring the peak current on each run.

Typically spark energies were in the range of 10-20 joules and efficiencies were in the range of 10-30%. No attempt was made in this study to optimize the spark input energy or the efficiency and the data do not show any strong correlation between energy, efficiency and pressure, although exceptionally high efficiencies such as the case above seem most likely to occur at the lower pressures and lower input energies. More typical values for runs at all pressures are closer to 15 joules in the spark with an efficiency of about 15% resulting in about 2.25 joules of Pressure-Volume energy in the bubble.

Liquids used for these experiments were chosen on the basis of optical transparency for photography and variation in physical properties which would give some assurance that the results could be applied to drilling muds. Water was used as a standard of comparison; the other liquids were a mixture of 50% water, 50% glycerin, and a mixture of 50% polymer solution, 50% glycerin. The polymer solution was 600 ppmw Polyox WSR 301 in water. Polyox is a Union Carbide brand name for polyethylene oxide, the WSR 301 has an average molecular weight of 2.4×10^6 . The glycerin-water mixture provides a Newtonian fluid with a density 13% higher than water and a viscosity at room temperature 6.7 times that of water, and within a factor of 10 of drilling fluid viscosities. The glycerin-polyox mixture has the same density (1.13 gm/cm^3) and is highly visco-elastic. The shear thinning behavior of drilling fluids was not modeled experimentally, but since both the theory and these experiments indicate the negligible importance of moderately high viscosity, the behavior of decreasing viscosity with increasing shear rate will have no measurable effect on overall bubble dynamics.

Data are shown in Figures 5 and 6. They present the data in dimensionless coordinates which allows comparison of bubbles of varying radii at different pressures. The reduced radius is normalized to the maximum radius

of the bubble and the reduced time is normalized to the theoretical Rayleigh collapse time, τ . The expression:

$$\tau = .915R \sqrt{\frac{\rho}{P}}, \quad \rho = \text{Fluid Density, } P = \text{Fluid Pressure}$$

can be obtained from equation (3) by solving for τ as a function of R and integrating. The maximum Radius and Rayleigh time for each run, along with the bubble's Pressure-Volume energy are given in Table 1. To give a clearer picture of how the histories vary with increasing pressure, the data for all 5 Glycerin-Polyox runs are presented in Figure 7 in dimensional coordinates of millimeters and microseconds.

The normalized data can be compared directly with the theoretical Rayleigh curve [Figure 1] and with Figure 2 which gives the theoretical collapse curves for both vapor filled theory and for bubbles containing non-condensable gas which causes the bubbles to rebound. The rebound portion of the curve would be the growth curve for a gas filled bubble. While the true behavior of the bubbles fits neither of these models exactly, they are convenient for discussing the data.

For all experimental runs, growth and collapse data tend to be bounded by the vapor and gas curves. In general growth portions of the data tend to be closer to the vapor curve and collapse data tend to be closer to the gas curve. In the denser liquids the asymmetry between growth and collapse tends to become greater with increasing pressure. This behavior of the data suggests that a good theoretical model for the overall bubble dynamics could be developed from a physical model which postulates a bubble containing both condensable vapor and non-condensable gas, with the non-condensable gas concentrated in an expanding core at the bubble's center. Since bubble histories are short compared to diffusion times, it is unlikely that the non-condensable gases from the spark ever become uniformly distributed in the bubble. Such a model is being developed and is expected to show the general Rayleigh like growth, gas like collapse behavior seen in these experiments. It should be noticed too that the data show a sharper cusp at rebound at minimum volume than does the simple gas filled model, which also fails to account for energy loss due to shock wave radiation and other effects in real bubbles where compressibility of the liquid becomes important during the last instants of collapse.

All data from the 50% glycerin-50% water runs [Figure 5] show a good fit to Rayleigh growth if the origin is shifted and the growth tends to become slightly retarded at increasing pressure, requiring a larger origin shift for a vapor fit. There is also a trend for the collapse portions of the data to become more retarded with increasing pressure. Thus the 1,000 psi data are an excellent fit to the vapor curve in both growth and collapse, while the collapse data become increasingly like the gas curve at higher pressures. A notable exception is the 3,000 psi run the data for

which fit the Rayleigh curve in both growth and collapse nearly as well as do the 1,000 psi data.

The glycerin-polyox data [Fig. 6] are much like glycerin-water data except that the trend for dynamics to vary from vapor like behavior to gas like behavior is uniform from 7 MPa to 35 MPa with no anomalies such as the run in glycerin-water at 21 MPa. The 7 MPa Glycerin-Polyox are the best fit to a Rayleigh model of all data with an origin shift of only .02 (compare .05-.15) and the data at 35 MPa lie on the vapor growth gas collapse curve with an origin shift of .15. It is possible that the non-Newtonian effects of the polymer are responsible for decreased sensitivity of the dynamics to random variations in the nature of the single spark discharge which probably account for the somewhat mixed behavior of bubbles in glycerin-water at the various pressures. It must be pointed out, however, that these differences in the data are small and should have little effect on the damaging capability of the bubble.

DAMAGE OBSERVATIONS AT HIGH PRESSURES

One inch fused quartz cubes were installed in the high pressure chamber adjacent to the spark gap and the high speed camera was used to record histories of bubbles growing and collapsing on a face of the cube. Records in both water and the glycerin-polyox mixture confirm that the qualitative features of bubbles collapsing on a boundary at pressures from 1,000 to 5,000 psi are the same as seen in studies at atmospheric pressure. Slight damage to the cubes can be seen in studies at atmospheric pressure. Slight damage to the cubes can be seen after only a few bubbles have collapsed on the surface. Exposure to approximately 50 bubbles produces extensive cracking of the quartz to a depth of about .5 cm. A photograph of the surface of a cube exposed to about 50 bubbles at 14 MPa ambient pressure is shown in Figure (8). The magnification is approximately ten. Continued exposure to collapsing cavities will shatter the cubes to destruction after about 100-150 bubbles. As in the studies at atmospheric pressure, some material is actually removed in the process, but for these brittle materials the greatest damage is in the extensive crack network that develops. It is also observed that there is a latent effect in the development of a crack network: the first bubbles may have little apparent effect, but continued exposure develops the major cracking that can appear suddenly and dramatically.

OBSERVATIONS ON THE LEACH AND WALKER NOZZLE

In the course of observing cavitation from nozzles such as the cavitjet it was thought to be of possible interest to look at the cavitation from a well-known nozzle such as the Leach and Walker design [24] which had a proven record of efficiency for operation in air at very high pressures. It, of course, was not, to our knowledge, designed for cavitating operation.

It was, therefore, mounted in the blow-down water tunnel with a jet of 30 meters per second submerged in essentially stagnant water about 1.2 cm from the target wall. Figure 9 shows three frames from a motion picture taken at 200,000 frames per second with the laser camera. Cavitation appears very stringy and ragged and there is little evidence of vortex core cavitation in this nozzle. The cavitation at the bottom of the frame was on the target plate and was unavoidable due to the difficulty in making the Leach and Walker nozzle cavitate. Its cavitation inception parameter was about 0.3 and it is unlikely that cavitation contributes to the effectiveness of this nozzle in practice.

OBSERVATION OF BUBBLES IN A STAGNATION FLOW

Preliminary studies of bubble behavior in a stagnation flow were made in the blow-down water tunnel facility. The tunnel has a vertical 7 cm x 7 cm square lucite experimental section and provides turbulence free flows of uniform velocity profiles up to about 30 meters/sec. A model was designed and installed in the experimental section for the stagnation flow studies. The nose of the model is a flat surface, normal to the flow, about 2.2 cm in diameter, and has a lithium-niobate piezoelectric gage just under the flat surface to detect and measure the stress pulses from collapsing bubbles. Bubbles are generated by an adjustable spark probe installed upstream from the model. The experimental set up is shown in Figures 10 and 11. The flow carries the spark generated bubble into the stagnation region where it can collapse on the flat surface.

To evaluate the feasibility of using bubbles to assist deep drilling it was felt that answering two questions experimentally had high priority: 1) could bubbles overcome the adverse pressure gradient of the flow to penetrate the stagnation region and collapse on the surface? 2) Would favorable bubble geometry be preserved which would result in the formation of the damaging micro jets when the bubble collapsed?

The answer to both of these questions is affirmative. Figure 12 shows a double exposure sequence of a single bubble generated by a spark on the axis of symmetry .65 cm above the flat surface. The first exposure was made 200 μ s after the spark and the second exposure 400 μ s after the spark. During the interval between the spark and the first exposure the average velocity of the bubble centroid was 415 cm/sec and its average velocity between the first and second exposure is 470 cm/sec. During this interval it has collapsed to about 40% of its first exposure volume. The collapsing bubble is thus accelerating into the stagnation region as predicted by the theory of Benjamin and Ellis, conserving its virtual momentum as it collapses. Other photographs have shown the bubbles collapsing on the surface with various combinations of standoff distance and tunnel velocity, and these collapses produce

the characteristic large stress spikes in the piezoelectric gage. The geometry of the bubble shape is also favorable. It is seen that the bubble deforms to an oblate ellipsoid. Its aspect ratio is 1:1.16 in the first exposure and 1:1.38 in the second.

When Naudé and Ellis published the first theoretical work on the geometry of initially spherical bubbles collapsing on a surface in the absence of flow, the predicted jets formed were slower than would be expected from damage studies. More recently the Russian workers Voinov and Voinov [5] showed theoretically by numerical calculations that if the initial bubble shape was an oblate ellipsoid, the predicted micro jets would have extremely high velocities, and this is the shape which is seen experimentally in the stagnation flow.

With these observations it was felt that attention should be shifted to the use of the high speed camera. Results are shown in a cinema to be presented at this meeting.

DEVELOPMENT OF LASER CAMERA

To obtain the desired photographic histories of the cavity growth and collapse, a new high speed laser camera was designed to the following approximate specifications:

Frame rate: Variable 10^3 to 2×10^6 frames/sec
Exposure time: <30 nanoseconds
Number of frames: >100 full frames or 200 half frames on 35 mm film
Frame rate: 100,000 to 1,000,000 per second
Frame size: .2 cm
Magnification: Variable 1/2 to 2
Working distance: 1 meter at maximum magnification.

The camera consists of a high repetition rate pulse locked ruby laser light source which frames an image scanned over a stationary strip of 35 mm film by a rotating mirror mounted on an air driven turbine.

The laser system is a new and improved high output version of a pulse locked laser system first developed by A.T. Ellis. The ruby is a 3/8 inch by 6 inches holographic grade rod with antireflectively coated, normally cut ends. It is pumped by two helical flashlamps in a reflective aluminum housing.

While the camera was built expressly for the bubble studies, it should find application to many research problems. The key to its versatility is the high intensity of the pulse locked laser system which allows the high effective f number of the camera optics (f 60). Additional flexibility is provided by the modular design which is centered on the turbine housing, a strong rigid structure of 1/2 inch aluminum plate to which bolt the auxiliary mirror housing, lens mount, and film quadrant; all of which are simple plywood structures. Thus modifications can easily be made such as film quadrants of different radii, lenses of different focal lengths, incorporation of a schlieren stop,

changes in auxiliary mirror geometry, or operation without an auxiliary mirror for a short focal length low f number configuration which would be useful for short histories at lower frame rates with a conventional light source. Transfer lenses could be installed in film quadrants and the camera operated as a Beckman-type camera with a continuous light source, or at high frame rates with the pulse locked ruby when a high intensity coherent light source is desired.

Photographs of the camera and laser head are shown in Figures 13 and 14.

SUMMARY

The objective of this study was to determine the feasibility of a new method for high-speed drilling of deep holes to permit more rapid and economical utilization of geothermal energy and petroleum resources. The method consisted of generating an electrical spark in drilling liquid and utilizing the high velocity jets and shock waves from the collapsing cavity to fracture rock than rely on the spark generated shock wave alone as had been investigated by others. This completely new approach required unavailable basic observations on bubble dynamics at high ambient pressures in order to establish a reliable mathematical theory for future design. Complete bubble lifetimes as short as 25 millionths of a second mandated the conception and development of a new ruby laser light source and camera. Although a considerable portion of project time was required, this system as an absolute necessity for completion of the project and is currently unique. Typically, 100 photographs at 3 microsecond intervals and 20 nanosecond exposure times were used for data acquisition. A narrow band light filter together with the optically coherent illumination revealed details of shock wave propagation and cavity geometry during the actual spark discharge which lasted for the first 5 microseconds.

Some principal findings are:

1. Damage to the solid occurs at bubble collapse and not from the spark generated shock waves.
2. Bubble dynamics agree with theory developed and may be predicted even at high ambient pressures above the critical point (22 MPa for water). (Observed to 35 MPa).
3. Inertial effects override the effects of viscosity and viscoelasticity on bubble dynamics and therefore existing drilling muds should not be less damaging than water. (Their higher density should make them more damaging). Experimental observations which support this conclusion were made for 50% glycerine-water mixtures as well as polymer solutions.
4. Photographs of shock waves incident bubbles show that there is negligible effect on the bubble for the short duration of the

shock. This contradicts ideas prevalent before this work was done but simplified theoretical predictions. The work does show longer time pressure oscillations in the simulated borehole which could help maintain cavitation.

5. Measurements show about 18% of electrical energy in the spark being recovered as bubble (PV) energy. This was essentially independent of ambient pressure (measured to 5,000 psi).

6. The pressure gradients in a stagnation flow which would be encountered in the jet from a drill bit nozzle have a favorable effect on bubble geometry and should enhance the damage capability of the collapsing cavities.

7. This study shows the introduction of cavities into drilling fluid will produce desirable increases of rock fracture even at high ambient pressure. This was a major unresolved question before this project was completed.

8. It was found that the electrical energy must be introduced in a short time relative to bubble lifetimes in order to produce an effective collapse. At 5,000 psi the 5 microsecond duration of the discharge was already becoming too long for the 25 microsecond lifetime.

RECOMMENDATION

Cavitation introduced into drilling fluid will substantially assist existing drill bits but possible methods of generating cavitation by utilizing flow energy from the mud pumps should be thoroughly investigated at high ambient pressures before any more effort is put into the spark generating method. The spark method has proved useful as a laboratory means of checking cavitation theory but there exist major technical difficulties requiring major engineering effort before field use could be accomplished.

REFERENCES

1. G.F. Naudé and A.T. Ellis, "On the Mechanism of Cavitation Damage by Non-hemispherical Cavities Collapsing in Contact with Solid Boundary," Trans. of ASME Journal of Basic Engineering, Vol. 83D, No. 4, pp. 648-656, Dec. (1961).
2. T.B. Benjamin and A.T. Ellis, "The Collapse of Cavitation Bubbles and the Pressures Thereby Produced Against Solid Boundaries," Phil. Trans. of the Royal Society of London, Series A, No. 1110, Vol. 260, pp. 221-240 July (1966).
3. F.P. Bowden, "The Formation of Microjets," Phil. Trans. of the Royal Society of London, Series A, No. 1110, Vol. 260, pp. 94-95, July (1966).
4. M.S. Plesset and R.B. Chapman, "Collapse of an Initially Spherical Vapor Cavity in the Neighborhood of a Solid Boundary," J. Fluid Mech., 27, 293 (1967).

5. O. Voinov and V. Voinov, "On the Process of Collapse of a Cavitation Bubble near a Wall and the Formation of a Cumulative Jet," Sov. Phys. Dokl., Vol. 21, No. 3, March (1976).
6. L. Euler, Hist. Acad. Roy. Science et Belles Lettres, Vol. 10, No. 227, (1754).
7. G.I. Taylor, "A Formulation of Mr. Tuck's Conception of Munroe Jets," Scientific Papers of G.I. Taylor, Vol. III, Cambridge University Press (1963).
8. G. Birkhoff, D.P. MacDougall, E.M. Pugh, and G.I. Taylor, "Explosives with Lined Cavities," J. of Appl. Phys., Vol. XIX, p. 563 (1948).
9. Lord Rayleigh, "On the Pressure Developed in a Liquid During the Collapse of a Spherical Cavity," Philosophical Magazine, Vol. XXXIV, pp. 94-98 (1917).
10. M.S. Plesset, "Dynamics of Cavitation Bubbles," J. of Appl. Mech., Vol. 16, p. 277 (1949).
11. M. Kornfeld and L. Suvorov, "On the Destructive Action of Cavitation," J. of Appl. Phys., Vol. 15, No. 6, pp. 495-496 (1944).
12. A.T. Ellis, "Techniques for Pressure Pulse Measurements and High Speed Photography in Ultrasonic Cavitation," Paper No. 3 in Cavitation in Hydrodynamics, Her Majesty's Stationery Office, London (1956).
13. C.F. Naudé and A.T. Ellis, "On the Mechanism of Cavitation Damage by Nonhemispherical Cavities Collapsing in Contact with Solid Boundary," Trans. of ASME, J. of Basic Engineering, Vol. 33D, No. 4, pp. 648-656, Dec. (1961).
14. M.S. Plesset and T.P. Mitchell, "On the Stability of the Spherical Shape of a Vapor Cavity in a Liquid," Q. of Appl. Mech., Vol. 13, pp. 419-430 (1956).
15. V. Johnson, R. Kohl, A. Thiruvengadam, and A. Conn, First International Symposium on Jet Cutting Technology, April 5-7 (1972) Coventry, England.
16. A.F. Conn and V. Johnson, Second International Symposium on Jet Cutting Technology, April 2-4 (1974) Cambridge, England.
17. (See Reference No. 2).
18. R.T. Knapp, "Recent Investigations of the Mechanics of Cavitation and Cavitation Damage," Trans. of the ASME, Vol. 77, pp. 1045-1054, Oct. (1955).
19. P. Gruber, "Formation of Jets by Impulsive Acceleration of a Curved Free Surface," Ph.D. dissertation, California Institute of Technology (1968).
20. J.G. Oldroyd, "Non-Newtonian Effects in Steady Motion of Some Idealized Elastico-Viscous Liquids," Proc. Roy. Soc. of London, Feb. (1958).
21. A.T. Ellis and R.Y. Ting, "Non-Newtonian Effects on Flow Generated Cavitation in a Changing Pressure Field," International Symposium on the Fluid Mechanics and Design of Turbomachinery, Penn State University, Sponsored by NASA and ONR, Aug. 31-Sept. 3 (1970) (available from U.S. Government Printing Office).
22. R.Y. Ting, "Cavitation Dynamics and Flow Fields in Dilute Polymer Solutions," Ph.D. dissertation, University of California, San Diego (1971).
23. J.L. Lumley, "Drag Reduction by Additives," Annual Review of Fluid Mechanics, Vol. 1, p. 367, Stanford University Press, Palo Alto, California (1970).
24. S.J. Leach and G.L. Walker, "Some Aspects of Rock Cutting by High Speed Water Jets," Phil. Trans. of the Royal Society of London, Series A, No. 1110, Vol. 260, pp. 295-308, July (1966).

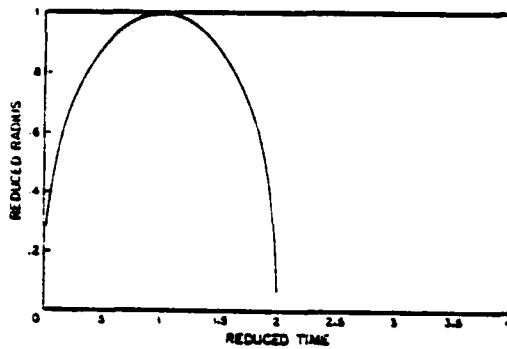


Fig. 1 Rayleigh Theoretical Curve

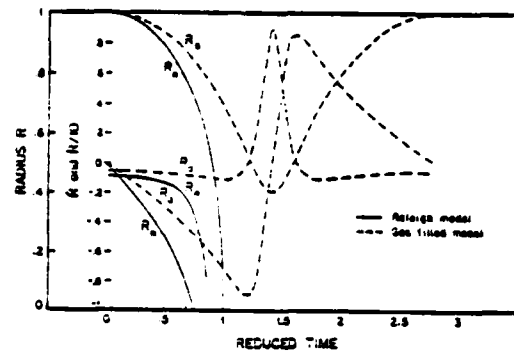


Fig. 2 Theoretical Collapse Curves

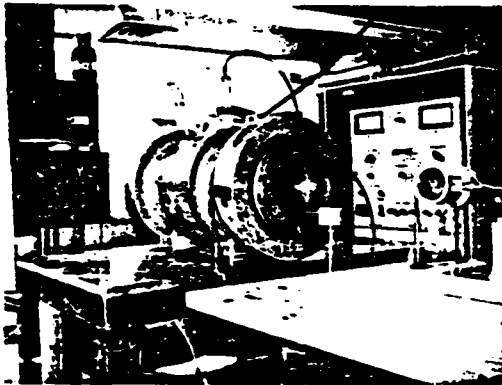


Fig. 3 Experimental Chamber

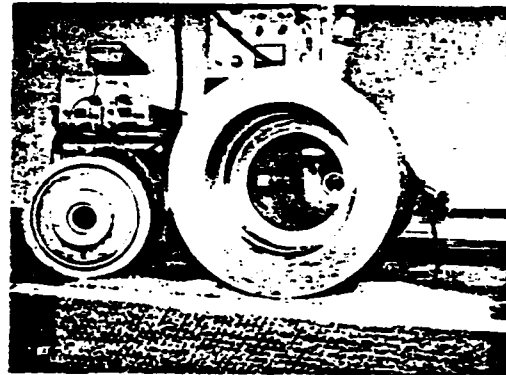
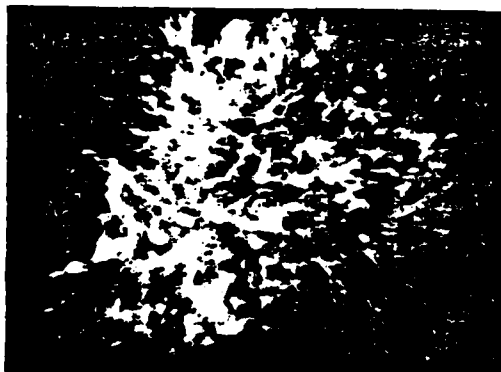
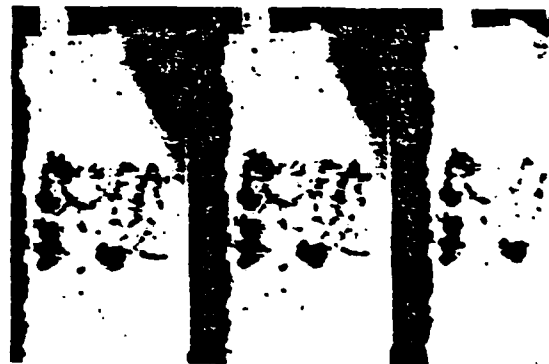


Fig. 4 Interior of the Experimental Chamber

Fig. 8 Surface of Fused Quartz Cube
Damaged by Bubbles at 14 MPa
Magnification 10×Fig. 9 Cavitating Jet from Leach and Walker
Nozzle 2×10^5 Frames per Second
Magnification 3×

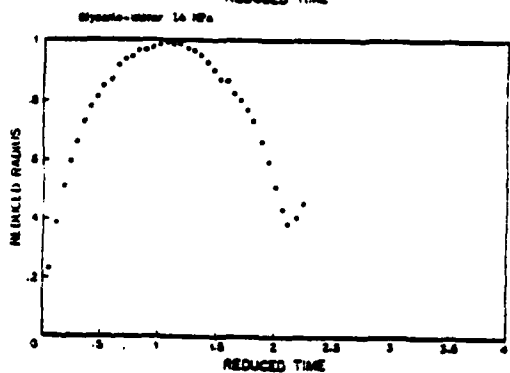
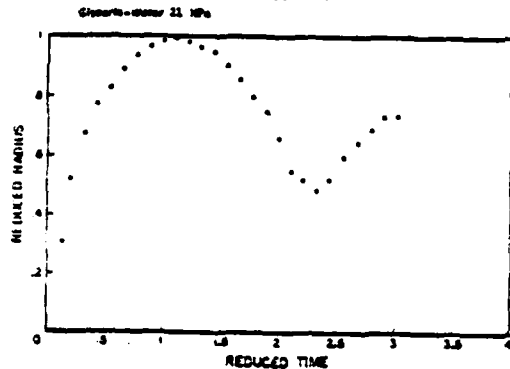
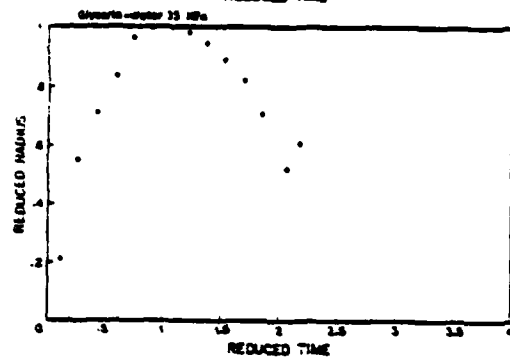
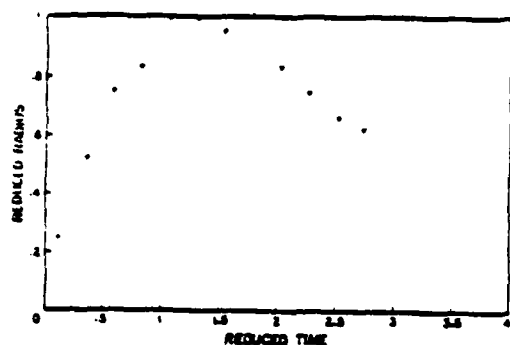


Fig. 5 Glycine-Water 7 MPa

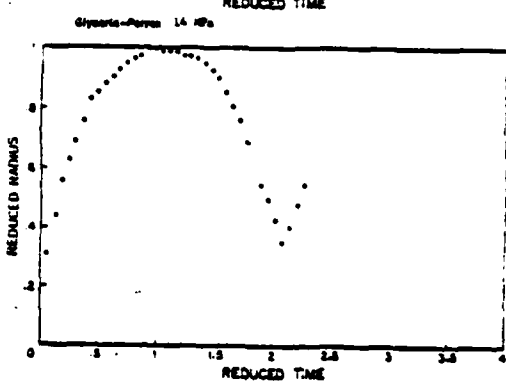
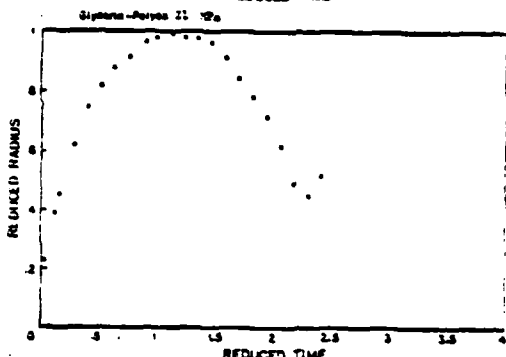
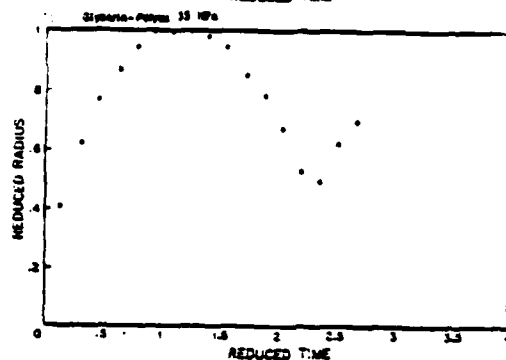
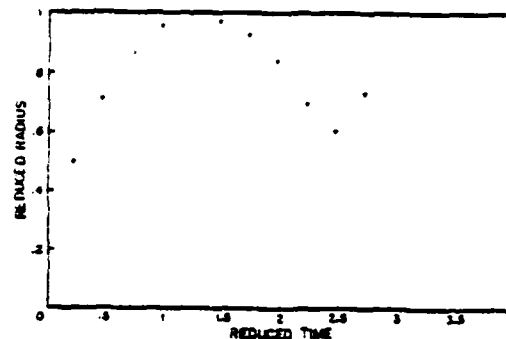


Fig. 6 Glycine-Polya 7 MPa

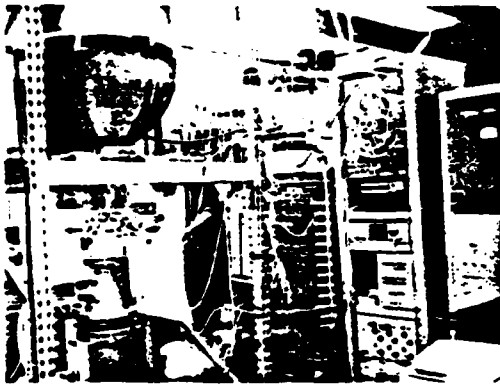


Fig. 10 Slow-down Water Tunnel Facility

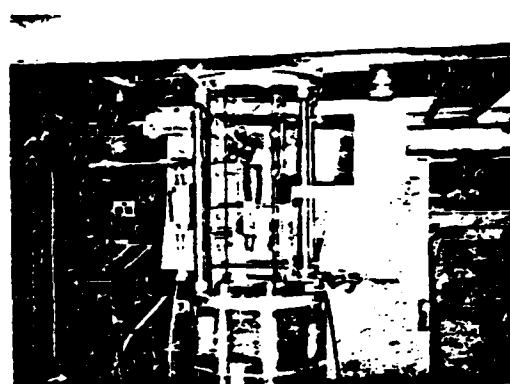


Fig. 11 Experimental Section of Slow-down Tunnel

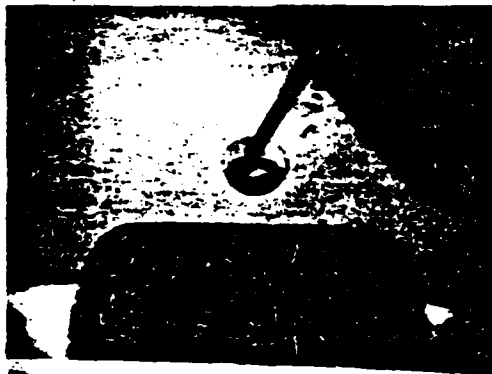
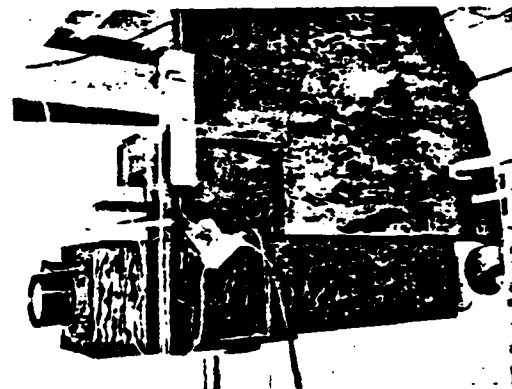
Fig. 12 Exposures at 200 μ s and 400 μ s of a Bubble Generated .65 cm Above Model Nose

Fig. 13 Camera Turbine Housing with Lens



Fig. 14 Pulse Locked Laser System. Visible from Left to Right: Photodiode and Beam Splitter for Monitoring Output, Output mirror, Kerr Cell, Polarizer, Ruby/Flashlamp Housing, Rear Mirror

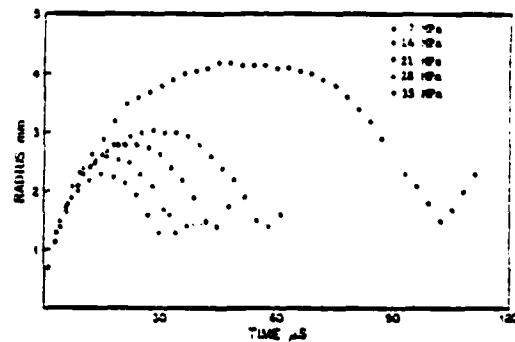


Fig. 7 System Polysen

UNIVERSITY OF CALIFORNIA
SAN DIEGO

Bubble Dynamics in Sagnation Flow

A dissertation submitted in partial satisfaction of the
requirements for the degree Doctor of Philosophy
in Engineering Sciences

by

John E. Sarrett, Jr.

Committee in charge:

Professor Albert T. Ellis, Chair
Professor Gilbert A. Hegemier
Professor Donald R. Smith
Professor Charles W. Van Atta
Dr. Frank B. Thiele

1982

Copyright 1982
by
John E. Sarrett, Jr.

The dissertation of John E. Starrett, Jr. is approved,
and it is acceptable in quality and form for

publication on microfilm:

Charles W. Van Atta

Robert H. Hargrave

Donald L. Smith

Frank S. Thies

Albert T. Ellis

Chair

University of California, San Diego

1982

iii

To my mother,

Elizabeth Starrett Fodlesak

And to the memory of my father,

John Elliott Starrett

iv

TABLE OF CONTENTS

List of Figures and Tables	vi
Acknowledgments	viii
Vita, Publications and Fields of Study	x
Abstract	xi
Chapter I. Introduction and Historical Background	1
Chapter II. Experimental Technique	9
Chapter III. Experimental Results and Discussion	20
Chapter IV. Theory of the Bubble Motion	46
Chapter V. Bubble Momentum	65
References	94

LIST OF FIGURES AND TABLES

Figure		Page
2.1	Experimental Schematic	75
2.2	Experimental Setup	76
2.3	Model in Working Section	76
2.4	Model Prior to Assembly	77
2.5	Pulse Locked Ruby Laser	77
2.6	High Speed Camera	77
3.1	Bubble 1 Oscillogram and Cine Sequences	78
3.2	Bubble 2 Oscillogram and Cine Sequences	79
3.3	Bubble 3 Complete Cine History	80
3.4	Bubble 4 Collapse Cine Sequence	81
3.5	Bubble 5 Collapse Cine Sequence	82
3.6	Bubble 6 Collapse Cine Sequence	83
3.7	Bubble 7 Motion History	84
3.8	Bubble 8 Motion History	85
3.9a	Bubble 9 Motion History	86
3.9b	Bubble 9 Dimensionless Radius and Virtual Mass	87
3.9c	Bubble 9 Dimensionless Centroid Position and Velocity	88
3.10	Centerline Velocity	89
4.1	Coordinate System	90
5.1	Dimensionless Force and Virtual Momentum Bubble 7	91

Figure

5.2	Dimensionless Force and Virtual Momentum Bubble 8	92
5.3	Dimensionless Force and Virtual Momentum Bubble 9	93
Table		
3.1	Bubble and Flow Parameters	45
5.1	Dimensionless Force Ratio	73

ACKNOWLEDGMENTS

To Professor Albert T. Ellis, I extend my deepest thanks. His kindness, encouragement, and insight have guided this research, and the opportunity of working with him is a privilege for which I will always be grateful.

I would also like to express my appreciation to Professors Gilbert A. Hegemier, Donald R. Smith, Charles W. Van Atta, and Frank B. Thies for serving on my committee and for generously giving their time and knowledge. My special thanks, too, to Professor Robert A. Swanson for inducing me to come to San Diego, and for countless discussions on a variety of subjects.

Experimental science leans heavily on the support of machinists and technicians, and I am indebted to Messrs. Jon B. Haugdahl, Ray E. Hummer, Wendell T. Hupp, Dean W. Newton, and Joseph R. Robison for their material assistance and for sharing with me their hard won craft.

Having worked as an administrator, I am acutely aware of the often unsung contribution to research made by administrative personnel, and so would like to thank especially Mrs. Ramona F. Carlson, Mrs. Barbara S. Fleming, Mrs. Ruth M. Sorenson and all of the AMES administrative staff.

Input from fellow graduate students and colleagues has also

been invaluable, and particular mention should be made of several rewarding discussions with Mr. Alan Bernath and with Mr. David W. Lischer.

For assistance with the final manuscript, my sincere thanks go to several people. Ms. Donna M. Jones provided expert and time consuming help in preparation of the photographic prints which were flawlessly reproduced in halftones at Van Veen Press by Mrs. Ann Van Veen and Mr. Mark Van Veen, who had earlier assisted in the construction of the high speed camera. The line drawings were accurately and aesthetically rendered by Ms. Allegra L. Pajot. And for the beautiful execution of the typescript and final preparation of the entire manuscript my thanks to Ms. Ametta R. Whiteman who is deservedly something of a legend at UCSD. The laborious proofing of the manuscript fell to my wife, Jane, who undertook this task repeatedly, tirelessly, and cheerfully.

For financial support of the experimental phase of this research, I gratefully acknowledge the National Science Foundation, and the Office of Naval Research.

Finally, I owe much to the continued confidence of my friends and family, but especially to my mother and to my wife without whose support and understanding this work could not have been completed.

VITA

August 22, 1942 - Born - Evanston, Illinois
1961-1963 Cornell University
1964-1969 Staff, Enrico Fermi Institute, University of Chicago
1969-1971 University of California, San Diego
1971 B. A., University of California, San Diego
1971-1980 Research Assistant, University of California, San Diego
1982 Doctor of Philosophy, University of California, San Diego

PUBLICATIONS

"Observations on the Role of Cavitation in Electric Spark Rock Drilling," with A. T. Ellis, Proceedings of the Seventeenth U.S. Symposium on Rock Mechanics (National Academy of Science, National Research Council, Addendum 6, "Fracture," August 1976), 1-7.

"Observations on Bubble Dynamics in Jet Flows and at High Ambient Pressures," with A. T. Ellis, Proceedings of the Fifth International Conference on Erosion by Liquid and Solid Impact (Cambridge Laboratory, University of Cambridge, England, September 1979), 57-1 to 57-10.

FIELDS OF STUDY

Major Field: Engineering

Studies in Applied Mathematics

Professors T. T. Frankel, J. W. Miles, D. R. Smith, and F. B. Thiele

Studies in Fluid Mechanics

Professors A. T. Ellis, P. A. Libby, C. W. Van Atta

Studies in Solid Mechanics

Professors A. T. Ellis, G. A. Hegemler, E. Reissner

Studies in Electrodynamics

Professor R. A. Swanson

ABSTRACT OF THE DISSERTATION

Bubble Dynamics in Stagnation Flow

by

John E. Sarrett, Jr.

Doctor of Philosophy in Engineering Sciences

University of California, San Diego, 1982

Professor Albert T. Ellis, Chair

The dynamic behavior of spark generated cavitation bubbles in an experimental stagnation flow is studied with high speed cine photography. It is found, in certain cases, that bubbles which would not collapse on the boundary in the absence of flow are carried to it by the stagnation flow, accelerating into the boundary on collapse. Further, bubbles in stagnation flow acquire an oblate spheroidal form which can result in very high velocity micro jets directed at the boundary on collapse. Impulses to the boundary from an imploding bubble is measured with a piezoelectric gage.

Not all bubbles accelerate into the stagnation zone however; some are repelled by their buoyancy in the pressure gradient,

while others experience a balance between buoyancy and the attractive Bjerknes force and undergo no acceleration at all. A theory is developed to account for the translational motion and it is found that a bubble's behavior is predicted by a dimensionless ratio of the forces acting on it at maximum radius.

even earlier Galileo [1638] had considered the failure of water in tension responsible for the mysterious inability of pumps to lift a column of water higher than thirty-four feet.

General interest in the problem, however, came with the advent of screw propeller steamships in the latter part of the nineteenth century. Two of the earliest papers on the subject were by Osborne Reynolds [1873, 1874] who sought to explain "The tendency which the screws of steamships have, under certain circumstances, to lose their hold on the water, and consequently to let the engines start off at a great speed" Based on experiments with model boats he believed the cause to be admission of air to the propellers. The discussions of these papers are interesting as well; William Froude expressed doubt that air could reach a deeply immersed propeller, and in a comment on the second paper Gray gave what must be one of the first descriptions of cavitation damage to a cast iron propeller: " . . . after it has been working some time it is invariably eaten into holes in that place which would be most exposed to that action." The action referred to being exposure to air. (The idea that damage was primarily due to chemical corrosion persisted into this century [see Flessa and Ellis 1955] .)

Twenty years later Reynolds [1894] made the first laboratory observations of water cavitating in a glass Venturi tube. He noted the cloud of bubbles at the contraction and attributed the hissing sound

CHAPTER I

INTRODUCTION AND HISTORICAL BACKGROUND

The study of single bubble dynamics is motivated, in large part, by the extraordinary ability of collapsing cavitation bubbles to damage solid materials. Cavitation is defined as the presence of a vapor phase in a flowing liquid and generally occurs if the minimum pressure in the liquid falls below its saturation vapor pressure, at which point the liquid boils forming vapor pockets called cavities. Depending on the nature of the flow and the bounding surfaces the cavities may be individual bubbles or a variety of other forms such as vortex cores, large quasi-stationary pockets, sheets, or streaks, which in turn may break up into individual bubbles. Subsequently swept by the flow into regions of higher pressure, the bubbles become unstable and their ultimate collapse is often a violent implosion which, if adjacent to a solid boundary, can have enormous destructive effect.

Perhaps the earliest clear theoretical recognition of cavitation was by Leonhard Euler [1754, p. 266]. As part of his analysis for the design of a reaction water turbine, he calculated that in the tubing of this machine the fluid pressure could become negative and warned that if negative pressures were allowed to occur a void would form at the walls of the tube. A translation of the relevant passage is given by Truesdell [1954, p. xlvii] who notes that d'Alembert also anticipated the onset of cavitation in his book on fluids in 1744. And

to the collapse of individual bubbles, in exact analogy with the hissing of water coming to boil in a kettle. About the same time R. E. Froude coined the word cavitation, apparently in a letter to C. Parsons regarding propeller performance on the Turbinia, the first steam turbine boat (see Morgan and Lichtman 1969).

The high propeller speeds of steam turbine ships caused continued interest in cavitation erosion which had been forestalled by improved alloys in propellers fitted to the slower reciprocating engines, but debate continued over whether the cause was mechanical or chemical. Silberrad [1912] reported severe damage to the propellers of the new ocean liners Mauretania and Lusitania which "would, had no remedy been found, have required replacing every few months." Mentioning also erosive destruction of water turbines, he concluded, based on metallurgical examination, that "erosion proper is a purely mechanical effect." In the same year Ramsey [1912] described damage to bronze propellers which occurred so rapidly "that the safety of the vessel may be jeopardized after only a few months, or even weeks of running." Attributing the damage to electrolytic corrosion, he made no mention of cavitation.

To resolve the issue the British Admiralty formed a committee in 1915 to investigate the subject. Their report (Parsons and Cook 1919) supported the mechanical view and focused attention on the collapse of individual cavities. The extensive experimental studies included a demonstration that collapse of a single cavity could

puncture 0.030 inch brass plate, implying pressures of 140 tons per square inch. In addition Cook did a mathematical analysis of the problem of spherical collapse arrested by a solid spherical boundary. He obtained what is now known as the Rayleigh equation and showed that such high pressures are indeed predicted.

Lord Rayleigh's interest in the problem grew both from Reynold's description and explanation of the sounds produced by water coming to a boil, and from the work of Parsons and Cook on propeller cavitation. Rayleigh [1917] extended Cook's analysis, based on the work of Besant [1859], and showed that extremely high pressures are generated near the wall of a collapsing spherical bubble even when its motion is not arrested by impacting a solid surface. He also allowed for the inclusion of permanent gas in the bubble, and, like Cook, gave some consideration to the compressibility of water, though analytical and experimental studies of shock waves from collapsing cavities came much later.

The Rayleigh theory describes the radially symmetric motion of an infinite ideal fluid, initially at rest, subsequent to the instantaneous appearance of a spherical bubble. Although the potentially high pressures predicted by the theory were long accepted as a basis for observed damage, it became increasingly apparent that most real cavitation damage involves translational motion of the bubbles and their collapse adjacent to a boundary, both of which make departure

from spherical symmetry inevitable. Nevertheless, as was shown by Plessett [1949], the volume growth and collapse of actual cavitation bubbles translating along solid boundaries can be reasonably well modeled by the Rayleigh theory if it is modified to allow for the changing pressure.

Wartime research on underwater explosions provided some of the earliest results on bubble motion, the influence of boundaries, and deformation of initially spherical bubbles. Of note is the study by G. I. Taylor [1943] who gave an analysis of motion based on the earlier work of Herring, and obtained photographic records of the motion and deformation of bubbles generated by electric sparks. These model cavitation bubbles closely, in contrast to explosion bubbles whose contraction is severely inhibited by the gaseous contents. Additional references to underwater explosion research are given by Cole [1948].

The nature of the final motion of collapse of cavitation bubbles, and consequently the actual mechanism of damage, depend strongly on the symmetry of the bubble. Kornfeld and Suvorov [1944] were the first to point out that asymmetry could account for damage from high velocity impact of the liquid on the boundary, free from objection to the unphysical situation posed by Cook. Their observation pointed toward the violent high speed micro jets which, it is now known, occur in several types of asymmetric collapse. Extended somewhat beyond

its range of validity, a perturbation analysis by Rattray [1951] implied the possible formation of re-entrant jets for bubbles collapsing near a boundary as well as for bubbles collapsing with translational motion. General consideration of the stability of spherical vapor cavities was given by Plessett and Mitchell [1956]. Extending the methods of their perturbation analysis, Naudé and Ellis [1961] did a theoretical and experimental study of the collapse of non-hemispherical bubbles in contact with a solid boundary. Their analysis clearly indicated jet formation, and their high speed photographic records of spark bubbles contained the first physical evidence that damaging high speed micro jets do occur with asymmetric collapse. These jets are analogous to the Monroe jets [Birkhoff, MacDougall, Fugh, and Taylor 1948] created by hollow cavities in high explosives, whose concentrated destructive effect has been known to mining engineers for over a century. While it is now widely accepted that such jetting is the primary mechanism of damage from collapsing bubbles, the shock waves that may occur can also have destructive effect. A discussion of their relative importance is given by Ellis [1966] which includes photographic examples of several collapse and jet formation modes as well as pictures of shock waves generated by ultrasonic cavitation which are among the first high speed cine photographs taken with ruby laser illumination.

The significance of stagnation flow where cavitation damage

occurs first became apparent in a series of experiments done by Knapp [1955]. He studied supercavitating flow past elongated, symmetric models in a high speed water tunnel. High speed cine photographs, taken while damage was occurring, identified the stagnation zone where the quasi-fixed main cavity (which originates at a minimum pressure region near the model's nose) re-attaches to the model downstream. At the same time small bubbles, their lifetime prolonged by proximity to the cavity's low pressure free surface, are carried into the stagnation zone where they collapse. Subsequent microscopic examination of the pitting of the model from the collapse of individual bubbles revealed not only that the pitting rate was greatest in the stagnation zone, but that it seemed to have a startling sixth power dependence on the flow velocity. Further, Knapp estimated that only one bubble in 30,000 actually damaged the surface.

General theoretical consideration of the effect of a bubble's translational motion on its eventual collapse was given by Benjamin and Ellis [1966], based on conservation of the fluid's momentum, or, more properly, its Kelvin impulse which can be identified with the bubble's virtual momentum. As it collapses the bubble accelerates in its direction of motion to conserve its virtual momentum; but if this momentum is sufficiently large, the Kelvin impulse on final collapse is manifested as vorticity in the fluid. The bubble folds in on itself to form a vortex ring, which, if conditions are right, takes the

form of a high speed jet piercing the bubble in its direction of motion. When this occurs with a bubble moving toward a solid boundary, the clear implication of its damaging potential can also be viewed in analogy with the impact of a solid projectile whose momentum is finally arrested by the boundary, with the force concentrated on a tiny area. Their theory emphasizes the importance of single bubble dynamics in the stagnation region, showing the need to understand the exact conditions which exist when damage is maximal.

CHAPTER II

EXPERIMENTAL TECHNIQUE

The growth and collapse of spark generated bubbles in an axisymmetric stagnation flow is studied experimentally in the transient working section of a blow down water tunnel. The stagnation region is created by a model installed in the working section which presents a flat, circular face perpendicular to, and on, the centerline of the flow. Just beneath the model's face, a piezoelectric crystal measures the stress pulse from a collapsing bubble. The spark gap which creates the bubble is formed by two adjustable electrodes upstream of the model.

Data taken on each experimental run include a high speed cine photographic history of the bubble, an oscilloscope record of the stress pulse from the piezoelectric gage, and a recording oscillograph strip chart which logs the operating pressures in the water tunnel that determine flow velocity and pressure at the stagnation point. Experimentally variable parameters include flow velocity and pressure, spark position and energy, cine frame rate and size, and overall event timing.

The experimental layout is diagrammed schematically in Figure 2.1. Figure 2.2 is a composite photograph of the actual set up. From left to right in Figure 2.2 are shown the capacitor bank, high

voltage power supply, and trigger circuitry for the pulse locked ruby laser, which is the light source for the high speed photography and is located just above the oscilloscope in the picture. The blow down water tunnel is in the center of the photograph. The rack to its right contains the recording oscillograph and the sequencer which operates the tunnel's solenoid valves, turns on and off the recording oscillograph, and provides an output signal indicating the tunnel is at operating speed. The next rack contains the high voltage supply, capacitors, and hydrogen thyratron discharge circuitry which constitute the spark pulser. One microsecond sparks in the water from the discharges of 0.01, 0.02, or 0.04 μF capacitors generate bubbles of three nominal energies. The high speed Ellis camera is on the bench at the far right.

Figure 2.3 shows two views of the model in the 7 cm x 7 cm lucite working section. On the left is a close-up of the view of Figure 2.2. The spark electrodes are seen entering opposite sides of the working section; they form a $\frac{1}{4}$ mm gap just above the flat face of the model. Also visible in this picture are the lens on the left which collimates the expanded beam from the laser, and the large gage below it which measures the pressure in the tunnel's compressed air reservoir. At the top front of the working section is the transducer which measures the free stream static pressure of the flow. Not shown is a similar transducer which measures the pressure in the

relatively quiescent water of the upper tank, which, with allowance for the hydrostatic head also gives the total pressure at the stagnation point on the model, by virtue of the Bernoulli equation. Together these transducers constitute a Venturi meter giving flow velocity, and their outputs go to the oscillograph. The picture on the right in Figure 2.3 is the view seen by the high speed camera. Clear in this view is one of the adjustable ball and socket holders for the spark probes which are 1.6 mm diameter thoriated tungsten welding electrodes, each tapered to a point. The cable which carries the signal from the crystal gage can be seen exiting the section through one of the model's tail fins. Figure 2.4 shows the brass model prior to assembly; the disc above the 1 inch mark on the scale is the piezoelectric pressure gage, a 19 mm x 2.34 mm Z cut lithium niobate crystal. The crystal seats 1.5 mm beneath the model's flat face which is 2.2 cm in diameter; the maximum diameter of the model is 3.1 cm.

The pulse locked ruby laser, shown in Figure 2.5, is the key element of the improved Ellis camera system which was newly designed and built for these studies and can operate in excess of one million frames per second. From left to right are the 100% rear mirror, Pockels cell, high power dielectric polarizer, flashlamp and ruby housing, and 60% output mirror. The overall cavity length is 60 cm. The polarizer is aligned with its direction of polarization parallel to the preferred polarization axis of the ruby, which is a

1 cm x 15 cm holographic grade rod with antireflectively coated, normally cut ends. It is pumped by two helical flashlamps in the reflective aluminum housing. The vertical channel in front of the laser holds the negative, beam expanding, lens. Not shown is a beam splitter which diverts a small portion of the light output into a fast photodiode to monitor the laser pulses, insuring a good photographic history is obtained. The Pockels cell pulser is visible in the rack behind the laser.

Operation of the laser involves what is believed to be a new method of employing a Pockels cell. It was discovered that if the optic axis of the Pockels cell is rotated slightly out of parallel with the ruby axis, the cell acts as a quarter wave plate with no applied voltage. This causes a 90° rotation of the light's polarization vector on two passes through the Pockels cell, effectively spilling the Q of the cavity. When a voltage of approximately 7.5 kV is applied to the cell the net rotation vanishes and the ruby is free to lase. Control of the cavity Q with this system is so strong that with no voltage on the Pockels cell the ruby will not lase even though it is pumped hard enough to lase on its secondary polarization axis in typical operation. A train of 90 ns wide 7.5 kV pulses applied to the Pockels cell at a frequency in the range of 10^5 - 10^6 Hz can cause the ruby output to lock onto the pulse frequency giving a train of light pulses of uniform height and 20 ns width. The width of the light pulses is independent

of the Pockels cell pulse width. The length and amplitude of the pulse train is governed by the length and amplitude of the capacitor bank discharge into the flashlamps.

The capacitor bank consists of 18 30 μF (10,000 volt) capacitors which can be connected to give variable capacitance up to 540 μF , the number being chosen to give the desired pulse train length. Inductors of approximately 400 μH between the capacitors give the discharge a reasonably uniform time profile. Together, the inductors and capacitors form a variable length lumped constant line. In typical operation at 200 kHz, 270 μF are used and the bank is charged to 7.5 kV. This yields about 300 frequency locked light output pulses of 0.01 joules each, giving about 3 millijoules/cm² of light on the film which is more than adequate for good exposures. Camera timing selects an optimum one millisecond portion of the pulse train for the photographic histories. The bank is discharged by a fast high current ignitron tube and associated trigger circuitry which also provides the pre-ionization pulse to the flashlamps.

Pulse locked lasing begins spontaneously after a predictable delay of approximately 500 μs from the trigger pulse to the ignitron. The Pockels cell pulse burst is begun at the same time the bank discharge is triggered. The Pockels cell pulses are generated by the gated output of a Hewlett-Packard model 214A pulse generator which drives the Pockels cell pulser. This pulser is a high power, two-

stage class C vacuum tube amplifier which delivers sufficient peak output current to drive the capacitance of the Pockels cell with the required fast rise time. Reliable pulse locking is critically dependent on all parameters of the system: bank capacitance and voltage relative to a given pulse rate; Pockels cell pulse shape; cavity dimensions and alignment; correct alignment of the polarizations of the ruby and polarizer; exact rotation of the Pockels cell axis; and temperature of the ruby which is methodically cooled with dry ice on the flashlamp housing between each run. The short exposure times of the ruby pulses frame sharp pictures of the bubble image as it is scanned at high speed over a stationary strip of 35 mm film by the rotating mirror of the camera. The parallel, coherent nature of the light provides the additional benefit of rendering visible the shock waves from collapsing bubbles which show clearly in the photographic histories.

Figure 2.6 shows the high speed camera. Light from the pulse locked laser passes through the experiment and into the camera lens. From the lens the light is reflected off an adjustable auxiliary mirror (visible inside the open access doors at the bottom) onto the rotating mirror (not visible) which sweeps the image over a stationary 90° arc of film positioned at a 152 cm radius from the axis of the rotating mirror. The near face of the lighttight plywood quadrant is removed in the photograph and the 240 cm long film track is visible

at its circumference. A viewing port in the film track can be seen at eye level. Film supply and take up magazines are mounted at either end of the track and are loaded with 100 foot rolls of Kodak Tri-X film providing 12 records per roll. A counter indicates the length of film transferred into the take up magazine. Initial alignment is accomplished by projecting a He-Ne laser beam from the viewing port backwards through the camera which is then positioned so the beam emerging from the lens is centered below the bubble spark gap and coincident with the alignment beam from the pulsed locked ruby. During operation the viewing port is used to log the date and time of the runs onto the film from the L. E. D. display of a digital watch. The lens is a 915 mm focal length aerial telephoto lens, mounted backward so its principle planes lie inside the camera. At the 1.5 meter working distance used, the image on the film is 91% full size. Covering the lens with a very narrow band 6943 Å filter (the ruby wavelength) allows open shutter operation with the room lights on and blocks the light from the spark as well.

The rotating mirror is one polished and plated face of a 2.34 cm aluminum cube mounted directly on the shaft of an air turbine, the unit dynamically balanced as a whole. The position of the mirror is identified by a scribe mark on the turbine rotor outside of the camera. The scribe mark is detected by an optical pickup which provides a pulse used both to monitor the turbine speed and, with the

tunnel sequencer signal, to provide a master trigger pulse for the experiment. The pickup assembly is mounted concentrically with the turbine axis and its position is azimuthally adjusted for a given turbine speed to provide the pulse typically 1000 μ s before the mirror face begins its scan of the film arc, thus allowing for the pumping time of the ruby and time for initial fluctuations in the light output to pass. The oscilloscope sweep and spark triggers are then delayed 1000 μ s so the bubble history starts at the beginning of the film record. Shorter spark delays permit observing the later successive rebounds of a bubble.

Calibration of the lithium niobate crystal gage is accomplished by carefully dropping a 1 gram stainless steel ball bearing on the face of the model and taking an oscillogram of the output signal from the crystal. Dropped from a height of 13 cm the impulse produces a signal whose time integral is 60 volt- μ s. The ball rebounds to a height of almost 10 cm indicating a change in momentum of 300 dyne-sec. Thus the constant for the gage is about 5×10^6 dynes/volt. This represents the integrated force over the whole crystal, and caution is taken in interpreting the bubble collapse pulses which are complex and due in part to jets and in part to shockwaves. Furthermore, there is some mechanical ringing in the signal and this calibration is taken only as a rough guide to the forces involved.

Tunnel pressure and velocity calibration is more exact. The fast, highly linear pressure transducers are variable reluctance

twisted Bourdon tube gages with dc outputs that are direct coupled through resistors to the appropriately chosen galvanometer is installed in the oscillograph. By statically pressurizing the whole system the oscillograph traces are calibrated against the precision Halse Bourdon tube gage used to set the pressure in the compressed air reservoir. The low range of pressure is double checked by putting a known hydrostatic head over the transducers.

An independent optical calibration of the velocity field is made with a dark field photographic technique using a 4×5 view camera. The flow is visualized with light scattered 90° by small polystyrene latex spheres in suspension in the water. The illumination is from a pulsed, short arc strobe lamp of 1-2 μ s flash duration. The light is focused and collimated into a thin sheet normal to the axis of the camera lens and on the centerline of the tunnel. During a run the lamp is flashed twenty times at a frequency of 8 kHz which is precisely measured with a quartz crystal frequency counter. The camera shutter is open to a single sheet of Polaroid film for the sequence of flashes, room lights out. A single polystyrene sphere in the flow thus appears as a string of twenty white dots against a dark field. The flow is steady for the short duration of a run so the string defines a streamline while the displacement between successive dots is proportional to the velocity. These displacements are measured on a precision measuring microscope.

Scale is obtained by measuring the image of a ground rod of known diameter photographed separately. The water tunnel is designed to give particularly uniform, turbulence free velocity profiles in the working section, and free stream velocities measured optically agree with the velocity obtained from the pressure traces to within a few percent in all cases and to within one percent for most runs. In addition the velocity field in the vicinity of the model can be checked. This is compared with the known potential flow solution for the flow past a flat disc perpendicular to a uniform stream, the limiting case of an oblate spheroid perpendicular to a stream [Milne-Thompson 1968, p. 499; Batchelor 1967, p. 457]. Given the free stream velocity, the calculated centerline velocity distribution for a 2.54 cm disc normal to the stream is in excellent agreement with the centerline velocity distribution measured optically. Off axis streamline shapes also check out well in the region near the center of the model face. Thus the velocity field in the experimental region is considered known from the transducer readings on the oscillograph chart. From the potential flow solution it can be shown that the centerline velocity is given by:

$$\frac{u}{U_\infty} = 1 - \frac{2}{\pi} \left[\frac{x}{1+x} + \tan^{-1} x \right] \quad (2, 1)$$

where U_∞ is the measured free stream velocity, u is the centerline velocity, $x = z/1.27$ cm, and z is the distance in cm along the

centerline, measured from the face of the model. For centerline distances from the model of 0.5 cm or less the distribution is a good approximation of an ideal stagnation flow. For the lowest experimental velocity the boundary layer thickness [Schlichting 1968, p. 91] on the model face is estimated to be only 0.04 mm and is ignored.

Metric calibration of the high speed photographic records requires both time and length scales be known. Time interval between frames is obtained simply by measuring the pulse interval of the Pockels cell pulse generator with a quartz crystal frequency counter and recording its value before and after each run. For the typical runs at 200 kHz the pulse interval is held to within 0.1% of its nominal 5 μ s value. Spatial scale is obtained from a grid of 1.00 mm squares ruled on a lucite plate with a milling machine and checked for accuracy with a measuring microscope. Installed on centerline in the water filled working section and photographed through the high speed camera, the grid covers the entire experimental region, providing calibration for measurement of the individual frames.

For analysis the film is projected onto a drawing board with the magnification adjusted such that the image of the 1 mm squares of the calibration grid falls exactly on the one inch lines of 10x10 to the inch square graph paper. There is no significant distortion of the grid. The high speed photographic histories are measured manually, frame by frame.

CHAPTER III

EXPERIMENTAL RESULTS AND DISCUSSION

Data from more than one hundred bubble histories record a continuum of dynamical behavior in the stagnation region, with free stream velocity from about 600 to 1800 cm/sec and total pressure at the stagnation point from about 100 to 300 kPa (~ 1 to 3 atm). Initial spark standoff distance from the model face varies from about 3 to 15 mm, and maximum bubble radius ranges from about 2.5 to 4.5 mm. Bubble size is varied by discharging either the 0.01, 0.02, or 0.04 μ F capacitor which is always charged to 13 kV. The spark discharges the capacitor only partially and the pressure-volume energy in the bubble is roughly 1% of the initial stored energy in the capacitor. The resulting nominal bubble energies are 8, 5, 17, and 34 millijoules, although these values can fluctuate more than 50% due to variation in the spark gap from imperfect adjustment, wear, and flow induced oscillation of the electrodes. Though generally placed on the axis of symmetry, the spark gap is deliberately moved up to 2.5 mm off centerline in several runs, confirming that observed behavior is not critically dependent on exact axisymmetry of the experiment. Tap water at 68°C filled the tunnel in the majority of experiments, but a few runs made in dilute polymer solution show no significant difference in bubble dynamics from those made in plain water. Histories obtained without operating the water tunnel allow

comparison with bubbles growing and collapsing in the absence of flow.

The data reveal a consistent pattern of behavior for a single bubble in a stagnation flow. During its growth and through the first part of its collapse, it deforms from an initially spherical shape into an oblate spheroid while moving toward the boundary at a more or less constant velocity that is less than the local stagnation flow velocity at the standoff distance. The oblate spheroid is elliptical in cross section with its major axis parallel to the boundary. In the latter stages of collapse the bubble forms a waist near its equator which grows increasingly pronounced, and often pinches off the bubble into two parts at the end of collapse. During this period of pronounced deformation, a bubble generated sufficiently close to the boundary will accelerate toward it while one too far away will decelerate and finally bounce away from the stagnation zone. There is also an intermediate case where the bubble continues its constant velocity motion toward the boundary through final collapse. A bubble generated very close to the boundary, of course, suffers early departure from ellipsoidal symmetry, becoming flattened on the bottom as it grows. Features of the full range of behavior are illustrated by the bubbles of Figures 3.1-3.9 and the parameters of these bubbles and the flows are summarized in Table 3.1.

Figures 3.1 and 3.2 show the striking contrast between the no

flow and stagnation flow cases for two otherwise similar bubbles generated just under 3 mm from the model face. Both figures show three 4 frame sequences from the high speed cine histories and the oscillogram of the signal from the lithium niobate crystal. The sequence on the left in each figure shows the bubble half way through its lifetime at approximately its maximum average radius. Blocking the light from the ruby laser, the bubbles appear black. The black strip at the bottom of each frame is the flat face of the model, and the black tapered line entering at an angle from the top of the frame is the image of the spark electrodes which are superposed in the camera's view. The sequence in the center of each figure shows the bubble 100 μ s before collapse and the sequence at the right captures the final collapse and the initial moments of rebound, which is due to small amounts of non condensed vapor or gas in the bubble. The scale of the cine photographs is 2 x actual size and the interval between frames is 5 microseconds; time proceeds from bottom to top in the sequences. The oscillograms are recorded with a horizontal time sweep of 100 μ s/division and cover the entire bubble history. The upper trace is the crystal signal whose vertical amplitude is 5 volts/division. The lower trace records the train of hair fine light pulses from the ruby which, though faint, are distinct in the original oscillograms.

Bubble No. 1, Figure 3.1 is the no flow case. The cine sequences, left to right, cover respectively the periods 310-325 μ s, 520-535 μ s, and 625-640 μ s of the bubble's history. Its maximum

average radius is about equal to the initial spark standoff distance (2.8 mm) and halfway through its life in the first sequence its centroid remains practically unmoved. It has undergone noticeable departure from spherical symmetry, however, and the flattening on the bubble's bottom is evident well before maximum radius in earlier portions of the cine history. The shape of the top portion of the bubble, nevertheless, shows a tendency to assume the prolate spheroidal shape predicted theoretically for an initially spherical bubble collapsing near a solid boundary in a liquid otherwise at rest [Rattray 1951, Chapman 1970, Plesset and Chapman 1971, Voinov and Voinov 1976]. The latter three studies use numerical solutions which permit following the bubble collapse to the point where the re-entrant jet strikes the boundary. They predict jet diameters on the order of the minimum cavity radius and jet velocities on the order of 100 m/sec for collapse under 1 atm ambient pressure which is the experimental pressure here. On the oscillogram of Figure 3.1 the collapse impulse is the small negative pulse which occurs about 2/3 of the way through the total record and is followed by mechanical ringing in the model. The thin negative going spike at the beginning of the record is electrical pickup from the spark and is followed immediately by a thicker but shorter spike due to the initial shock wave striking the model which is in turn followed by ringing. The time on the oscillograms can be resolved to a precision of about 2 μ s and careful

measurement shows the collapse pulse to occur at about 633 μ s which is just before the third frame from the bottom in the right hand cine sequence. The amplitude of the collapse pulse is about 1.7 volts; multiplying this by the gage constant (5×10^6 dynes/volt) the peak force on the model face is about 8.5×10^6 dynes (about 20 pounds). Although the collapse mode here does differ from the theoretical calculations, it seems reasonable to estimate that the jet diameter is on the order of 1 mm, and the area on which it acts is on the order of 1 mm^2 . This would imply a peak pressure on the boundary of 8.5×10^8 dynes/cm² = 84 MPa (about 12,000 psi) and below the yield strength of the brass model. Assuming this is due to ccv water hammer pressure, and taking the sound speed, c , as 1400 m/sec the implied jet velocity, v , is about 60 m/sec. This jet velocity and diameter are consistent both with the magnitude of the theoretical predictions, and the $\sim 7 \mu$ s width of the peak of the collapse pulse on the oscillogram which is on the order of the estimated jet radius divided by the estimated jet velocity. The size of the bubble and the absence of visible shockwaves also make it likely that the order of these estimates is correct.

Estimated jet impact pressure and velocity for Bubble 2.

Figure 3.2, are radically greater. Measurement of the oscillogram indicates that the jet strikes at 663 μ s, about 1-2 microseconds before the origin of the shockwaves which first appear in the second

frame from the bottom of the right hand sequence, at 666.5 μ s. (The cine time origin is accurately established by projecting back from the measured shockwave radius in the first frame of the history using the measured shock velocity.) The sharp jet impulse spike on the oscillogram measures 12.3 volts in amplitude indicating a force of more than 6×10^7 dynes (135 lbs). An estimate of the area over which this pressure acts is obtained from inspection of the model face (subsequent to removal from the tunnel) which reveals tiny pits $\sim 1/4$ mm diameter that can only be due to microjet impact from the collapse of individual bubbles. Taking the area as 5×10^{-4} cm² the impact pressure is in excess of 10^{11} dynes/cm² = 10^4 MPa (~ 1.5 million psi). The jet must be supersonic and assuming that 10^4 MPa = $1/2 \rho v^2$, the stagnation pressure of the jet, the velocity is estimated to be on the order of 5000 m/sec.

The stagnation flow responsible for the marked change in behavior of Bubble 2 relative to the no flow case is the lowest velocity flow used in these experiments, and results from letting the water in the upper tank fall under gravity alone without actually blowing the tunnel down. Free stream velocity is ~ 600 cm/sec and the centerline velocity at the position of the bubble's maximum radius centroid is ~ 150 cm/sec; but even these low velocities are sufficient to cause the ellipsoidal deformation evident in the left hand sequence (321.5-336.5 μ s) of Figure 3.2. It is this initial deformation which is largely

responsible for the distorted shape which is shown in the center sequence (556.5-571.5 μ s) and the consequent violent collapse in the right hand sequence (661.5-676.5 μ s).

Features of this bubble shape and the resultant high speed jetting were predicted theoretically by Voinov and Voinov [1976]. Obtaining a solution of the Laplace equation through the use of an Integral equation over the boundaries, their numerical method naturally introduces a higher density of support points near the axis of symmetry and is therefore particularly suited to the problem of a jetting bubble [Voinov and Voinov 1975]. Their calculations describe the collapse of an initially oblate ellipsoidal bubble near a solid boundary, and show that as the ratio of major to minor axes increases from 1:1 (the spherical case) up to $\sim 1.2:1$ the resulting jet increases rapidly in velocity and becomes thinner. Beyond 1.2:1 the phenomenon of pinching off occurs which results in a yet higher velocity jet as the bubble wall collides with itself from the annular closure of the waist or neck, in a manner that is in exact analogy to the formation of the destructive Monroe jets. For this mode of collapse they predict a jet velocity of several thousand meters per second, in accord with the experimentally based estimates of this work.

As with the no flow case, there are differences between the theoretical predictions and the experimental observations. A likely source of the discrepancy is that the theory in both cases treats a

bubble whose initial surface velocity is everywhere zero, in a liquid at rest. The experimental bubbles, though their rate of change of volume is zero at maximum radius, are still undergoing deformation in the stagnation flow. Further, experimental bubbles, which grow as well as collapse in proximity to the solid boundary, become flattened on the bottom when the initial spark standoff distance is on the order of the mean-maximum bubble radius. Although the critical top portion of the bubble in the center sequence of Figure 3.2 is very similar in shape to the theoretical profile, the real bubble is much flatter overall, and the distortion has developed somewhat differently. In the Voinov studies the pinching originates near the top of the bubble, while in the experimental bubble pinching first occurs near its equator during the time between the left and center sequences. The profile seen in the center sequence then develops because the top portion of the bubble collapses more rapidly than the bottom portion. The subsequent development of the upper part of this bubble between the center and right sequences is much like the case computed in the Voinov study for an initial major to minor axis ratio of 1.25:1, just beyond the ratio where annular flow starts to pinch off the top of the bubble. The experimental aspect ratio for this case is 1.4:1 at maximum size, but the final history of the bubble top is similar: by 620 μ s (the equivalent time of the final theoretical profile shown in the Voinov paper) the part of the bubble above the pinch has collapsed to a tiny pip which continues to shrink and is gone at 641.5 μ s.

Aside from reduction in volume the appearance of Bubble 2 changes little through the rest of the collapse.

Collapsing bubbles which acquire shapes that somewhat resemble those of Bubble 2 have been seen in other studies where an oblateness develops due to formation less than one maximum radius from a solid boundary. Benjamin and Ellis [1966, Fig. 5] show an example where the thin jet is clearly visible in the final stages of collapse. Moreover, like Bubble 2, the final form of this bubble when jetting occurs is a short right cylinder. The theoretical shape predicted by Naudé and Ellis [1961] also shows some of these features, but, as confirmed by their experimental studies, develops more like the lower aspect ratio bubbles of the Voinov study. Similar cavity forms have even been seen in flows tangential to the bounding surface [Ellis 1966, Figs. 1, 5] so it is probable that the flow in which a bubble is imbedded effects its mode of collapse only to the extent that it alters the bubble's geometry near maximum radius.

From the greater oblateness which occurs in the higher velocity stagnation flows, however, the final deformation becomes pronounced that the bubbles bear only distant resemblance to those of earlier studies. Figure 3.3 shows the complete growth and collapse history of a bubble (No. 3) in a stagnation flow whose velocity is twice that of the Bubble 2 flow. It is a larger bubble than Number 2 and its longer lifetime also contributes to the degree of deformation

which it undergoes; but unlike 2 the initial spark standoff is more than one maximum radius from the boundary and so No. 3 better exhibits features of a bubble moving toward the boundary. Also Bubble 3 is the one example shown in this work of a bubble generated in a dilute polymer solution. As in previous spark bubble-polymer studies [Ting 1971; Ellis and Starrett 1979], the 100 ppmw addition of Polyoxy WSR 301 to the water is found to have no effect on the experimental behavior other than making the bubble surface somewhat smoother, and inhibiting the natural cavitation which forms on the spark electrodes at the higher velocity flows. Both effects, however, improve the photographic quality of the cine sequence which is contact printed from the original 35 mm negative. Scale is 0.91 x actual size and the print is cropped into 12 vertical columns in the figure. Frame interval is again 5 μ s and time proceeds from bottom to top in each column and from left to right between columns, as is the case for all the histories shown in this work. Each of the 12 columns (except the first) contains 15 frames and the entire history covers 865 μ s from the "time = 0" frame which is the somewhat darkened frame in the first column. The reason for the darkening in this frame is unclear, but is probably a coincidental drop in the ruby output. The ball at the tip of the spark electrodes in this frame is not the bubble, but a feature of the initial spark and the spherical shock wave which signals the bubble's birth, and it is just preceded by a

thin shock which radiates from the entire length of the electrodes. Bubble 3, itself, is first seen in the next frame, 5 μ s into its life. Its collapse is complete at 810 μ s in the fourth frame from the bottom of the right hand column, where the extensive collapse shock system is seen. Measurement of the oscillogram which accompanies this history indicates that the jet strikes with a force of $\sim 9 \times 10^7$ dynes (~ 200 lbs) at 803-804 μ s which is just before the third frame from the bottom. Frames 5-15 of column 12 show the initial rebound of the bubble, but also record an interesting phenomenon frequently seen in the histories: the shock at 810 μ s precipitates the collapse of natural cavitation bubbles which shed from the spark electrodes in the flow. These collapsing bubbles in turn produce shock waves which can be seen originating near the electrodes and persist through $t = 835 \mu$ s. Clearly, however, the shock waves pass the majority of cavities without effect, and it is evidently only small cavities, or perhaps those already near collapse, which are imploded by shocks.

The main body of Bubble 3's history shows its motion toward the boundary and its steady deformation to oblate ellipsoidal shape which continues as the bubble passes through its maximum radius at about 365 μ s in the sixth column. Formation of the waist near the bubble's equator is first evident around 500 μ s in the eighth column, becoming increasingly pronounced through the remainder of the history. It is also seen that in the latter part of collapse the

acceleration of the bubble's centroid into the boundary is due in large part to the asymmetric deformation that develops as the portion of the bubble above the waist collapses more rapidly than the portion below. This tendency of the bubble to "self propel" through "skewness of form and velocity distribution" relative to its centroid was shown theoretically by Benjamin and Ellis [1966] to be a potentially important motion in the collapse of a translating cavity, contributing a term to the axial Kelvin impulse of the fluid through the far field dipole behavior of its velocity potential. Such skewness is evident in all the experimental bubbles which undergo translational acceleration during collapse, as shown by the cine sequences of Bubbles 4, 5, and 6 whose accelerations on final collapse are, respectively: away from the boundary; zero; and toward the boundary. Scale of the photographs for all three is 1.75:1.

Figure 3.4 shows the final collapse and initial rebound of Bubble 4 (407-522 μ s). Generated from an initial standoff of 9.6 mm in one of the highest velocity experimental flows (1840 cm/sec), it attains a maximum radius of 3.86 mm at 366.5 μ s into its life, where its aspect ratio is 1.3:1. As with all bubbles generated much over 6 mm from the model, its final motion is away from the model's face; and at 407 μ s, the first frame of Figure 4.3, it has already lost its 945 cm/sec velocity toward the boundary and is beginning its upward acceleration. Like Bubble 3, Bubble 4's final acceleration

results largely from its asymmetric deformation, but in this case it is the bottom portion of the bubble, below the waist, which collapses more rapidly. Final collapse, indicated by the shock system, occurs at about 460 μ s, just before the fourth frame in the center column. On rebound the Kelvin impulse is conserved by the vortex ring which can be seen edge on and somewhat twisted in the right hand column; its motion is upward, consistent with the final direction of the bubble's virtual momentum. Again, a sort of chain reaction of collapse of natural cavitation bubbles shredding from the spark probes is initiated by the collapse of Bubble 4, and the shock waves from one such collapse in the uppermost frames of the center column initiate yet another natural bubble collapse, evident in the third frame of the right hand column. In these experiments it is found that shock waves from flow produced cavities occur only when triggered by an initial shock.

As the ratio of a bubble's maximum radius to its distance from the boundary increases in a given flow, there is a transition from acceleration away from, to acceleration toward the boundary. This transition seems to be rather abrupt, but Bubble 5 in Figure 3.5 is one of the rare cases where the apparent forces acting on the bubble are so balanced that its translational velocity remains unchanged through both collapse and initial rebound. Further, such a bubble maintains a high degree of symmetry, assuming a characteristic hourglass or dumbbell shape that is predicted theoretically for

an initially oblate ellipsoidal bubble collapsing in an infinite liquid [Chapman 1970, Chapman and Plesset 1972]. Using a different numerical technique based on a variational approach developed by Hsieh [1972], Shima and Nakajima [1977] found the same shape in a symmetrically equivalent problem. The collapse of Bubble 5 shows no evidence of vortex ring formation or jetting, and while it could be supposed that its vanishing virtual momentum would be "conserved" by the Monroe type formation of equal and opposite jets, this is probably forbidden by the nearly cylindrical form of its waist just prior to collapse and the finite compressibility of the water [Walsh, Shreffler, and Willig 1953]. Bubble 5 begins from a standoff of 6.3 mm, reaching its maximum volume in 243 μ s at 5.5 mm from the boundary where its constant centroid velocity of 335 cm/sec is about equal to the local centerline velocity of the stagnation flow. Its aspect ratio is 1.16:1 at its maximum radius of 2.73 mm. Figure 3.5 shows the bubble from 442 to 557 μ s with the collapse shock first appearing in the fourth frame of the center column at 497 μ s.

Figure 3.6 covers the period from 592 to 707 μ s in the collapse of Bubble 6. This is another example of acceleration toward the boundary, but in this case the 5.1 mm initial standoff is sufficiently greater than its 3.85 mm maximum radius (reached at 326 μ s, aspect ratio 1.5:1) that it would not have collapsed on the model face without the stagnation flow. Having moved steadily toward the boundary at

375 cm/sec for the first 400 μ s of its life, the bubble centroid in the first frame of the sequence already has a velocity of about 1200 cm/sec which is roughly equal to both the free stream flow velocity and average wall velocity of the bubble, R_0/t_R , where R_0 is the maximum mean radius and t_R is the characteristic Rayleigh time which coincides with the experimentally observed time to reach maximum radius. The acceleration and growing skewness continue through the sequence; the top portion of the bubble has collapsed almost completely in the uppermost frame of the center column, and annular closure of the waist is indicated by the shock wave which is just touching the model face in the third frame from the bottom of the right hand column (the arrival of this shock at the model 4 μ s prior to jet impact leaves a clear signature on the oscillogram of the crystal signal). The fourth frame at 687 μ s shows the cavity 1 μ s after jet impact; also seen is a particularly nice example of a shock (from the waist closure) collapsing another cavity (on the tip of the spark electrode), an event which is clear from the tangency of the two shock waves. Peak force on jet impact from Bubble 6 measures $\sim 7 \times 10^7$ dynes; the main collapse shock system appears in the fifth frame at 692 μ s.

Flow velocities in the examples of Bubbles 3 and 6 are comparable, and it is of interest to contrast the extensive natural cavitation in water seen shedding from the electrodes in Figure 3.6 with the relatively meager cavitation evident in the polymer solution in Figure 3.3. Further, the full cine history of Bubble 6 shows substantial

natural cavitation throughout, while in Figure 3.3 the polymer solution cavitates appreciably only when the velocity near the electrodes is enhanced by the collapse of Bubble 3.

Of more importance to the present study, however, is the difference in the geometry of the two collapsing bubbles, which is due only to their relative proximity to the boundary. Bubble 3's shape is affected rather strongly by its closeness to the model face, while the final geometry of Bubble 6 is typical not only of bubbles which just reach the boundary on collapse, but of bubbles which accelerate toward the boundary without reaching it as well. Although the rounded bottom of Bubble 6 better reflects the general case than the flattened shape of Bubble 3, the similarities in form and development of the two are even more obvious, and are common to all bubbles which overcome buoyancy and accelerate toward the boundary on collapse.

A quantitative picture of bubble motion is better given by curves than photographs and the three modes of bubble behavior in stagnation flow are so illustrated in Figures 3.7, 3.8, and 3.9. These figures show the data for Bubbles 7, 8, and 9 as measured from the high speed cine histories. Only a representative number of the points actually measured are plotted in the figures, but the curves shown are faired through all the experimental points. With the exception of Figures 3.9b and 3.9c which are dimensionless, the abscissa of each figure is real time in microseconds; the ordinate in

millimeters refers to the mean bubble radius and to the distances from the model face of the bubble's centroid, and its upper and lower extremities. Until the final stages of collapse the bubble profiles are closely elliptical and the mean radius is taken as $(a^2b)^{1/3}$ where a is the semimajor axis, and b the semiminor axis of the ellipse. The aspect ratio a/b is given by the solid points and dashed curve labeled $10(a/b - 1)$, but here the ordinate is to be read as a dimensionless number. Thus, as an example, at $t = 200 \mu s$ in Figure 3.7, the ordinate of the dashed curve is 2 and so $a/b = 1.2$, the aspect ratio of Bubble 7 at $200 \mu s$.

Principal quantities pertaining to each figure are given in their upper right hand corners. Volume growth of all experimental bubbles nears exact match with Rayleigh theory and so time to reach maximum mean radius, R_0 , gives the characteristic Rayleigh time t_R . U_∞ is the free stream experimental velocity measured from the pressure transducer readings on the oscillograph chart. The bubble centroid velocity v_c refers only to the approximately constant velocity portion of the bubble motion and is also given as a fraction of the free stream velocity to facilitate comparison with the local velocity which can be found from Figure 3.10.

Figure 3.10, which is computed from equation (2.1), gives the centerline velocity distribution for all experimental runs. The dimensionless abscissa gives the local velocity, u^* , as a fraction of the

free stream velocity, and refers to the gradient of u^* and to the quasi-dimensionalless pressure gradient $u^* \frac{du^*}{dz}$ as well. The dashed lines give the corresponding values for u^* and its gradient for the idealized stagnation flow. The near unity value (1.003) of the gradient at $z=0$ is a numerical coincidence of the 2.54 cm diameter of the disc normal to the stream from which equation (2.1) is derived. It results in the unexpected convenience of unity slope for the ideal stagnation flow curve when z is expressed in centimeters, and when reading the figures the local centerline velocity u^* is given approximately (for $z < 5$ mm) by the numerical value of the distance from the boundary in centimeters.

Figure 3.7 is typical of bubbles generated at the greater standoff distances and, like Bubble 4, Bubble 7 bounces away from the stagnation zone on final collapse. The skewness it develops is evident from the position of its centroid. Midway between the upper and lower boundaries throughout most of the history, the centroid approaches the upper boundary near collapse. The dashed curve indicating aspect ratio is continued somewhat beyond the initial formation of the waist until the bubble is no longer roughly ellipsoidal. The irregularity in the early growth of the aspect ratio, a/b , is seen only in the large standoff cases, but is typical for these.

Figure 3.8 represents the history of Bubble 8 which, like Bubble 5, maintains both symmetry and constant centroid velocity

throughout its life. The point shown on the centroid curve at about 460 μ s is measured from the rebounding bubble, and all but the initial few points of the curve lie on a straight line whose 450 cm/sec slope matches the local stagnation flow velocity 3.9 mm from the model face. The brief period of deceleration following the birth of the bubble is a phenomenon commonly seen with bubbles generated on the order of 5 mm from the boundary. Also common to bubbles created in this intermediate standoff range is the fairly linear growth of the aspect ratio shown by the dashed line which is terminated in the figure at the point where Bubble 8 begins to acquire its final hourglass form.

The behavior of Bubble 9 (Figures 3.9a, b and c) is very similar to that of Bubble 6 and is characteristic of bubbles which accelerate into the stagnation zone on collapse. Generated in the same velocity field and at about the same standoff as No. 8, Bubble 9's greater relative size results in the motion shown in Figure 3.9a. The centroid curve shows a more pronounced initial deceleration than that of Bubble 8, and the steeper slope of the dashed curve indicates faster growth of the aspect ratio which levels off as Bubble 9 passes maximum radius. This curve is terminated at 450 μ s where the 1.6:1 ellipsoid is just beginning to develop a waist at its equator. Well before this time, however, the acceleration of the centroid has begun, as is evident from the greater negative slope of the upper bubble boundary curve relative to that of the lower bubble boundary which,

characteristically, approaches the model face more and more slowly as collapse proceeds. The final sharp acceleration of the centroid, though, is due to the rapid development of skewness in the bubble's shape as the portion of Bubble 9 above the pinched in waist shrinks more quickly than the portion below. At 622 μ s the oscillogram registers a peak force of nearly 6×10^7 dynes as the jet strikes the model face. The appearance of the bubble 3 μ s earlier in a frame of the cine history is much like that of Bubble 6 at 682 μ s in Figure 3. 6.

The upper curve of Figure 3. 9b shows the dimensionless radius-time history of Bubble 9. The axis is normalized with respect to the Rayleigh time, $t_R = 0.915 R_0 \sqrt{\rho/\Delta p}$. It is seen that the mean radius, R , develops in accord with Rayleigh theory through $t/t_R = 1.4$ where the Rayleigh collapse curve is shown with a dotted line. The extension of the bubble's lifetime is due principally to its proximity to the solid boundary as first shown by Rattray [1951], and is indicated by the numerical studies of bubbles collapsing near walls as well. The excellent fit to the Rayleigh curve through maximum radius obtains without modifying the theory to allow for the increasing pressure as the bubble moves toward the stagnation point. The Rayleigh times for all bubbles, which are measured from the cine histories, agree within about 7% or better with the time computed as $0.915 R_0 \sqrt{\rho/(p_0 - p_v)}$, where $p_v \approx 0$ is the vapor pressure and p_0 is the pressure in the stagnation flow at the position of the bubble's maximum radius centroid, and is found from the Bernoulli equation, equation (2. 1), and

the pressure transducer readings. Both p_0 and the corresponding flow velocity u_0 for Bubbles 1-9 are included in Table 3. 1.

The dimensionless virtual mass of Bubble 9, shown by the lower curve in Figure 3. 9b, is that of an oblate ellipsoid translating parallel to its axis in an infinite fluid. Writing the virtual mass as $K(R/R_0)^3$, K is given by the same potential flow solution used to find equation (2. 1). A somewhat involved formula for K as an explicit function of the ellipsoid's eccentricity may be found from the expression for the fluid's kinetic energy [Milne-Thompson 1968, p. 501], but when K is plotted as a function of a/b it falls on the straight line:

$$K = 0.615 \left(\frac{a}{b} \right) - 0.115 \quad (3. 1)$$

in the range $1 \leq a/b \leq 2$, which covers all of the experimental bubbles. The increasing value of K with time causes the virtual mass to peak somewhat beyond maximum radius. For a spherical bubble K would have a constant value of 0.5 and the virtual mass curve would be symmetric about $t/t_R = 1$.

Figure 3. 9c shows the dimensionless centroid position and velocity of Bubble 9. Writing z as the distance from the model face, $\dot{z} = z/R_0$ and the velocity is $d\dot{z}/dt$ where $\dot{t} = t/t_R$ as in the previous figure. Dashed lines give the corresponding quantities for a particle convecting along the centerline of the stagnation flow in the absence of the bubble, and are calculated from equation (2. 1). Because the

kinematical boundary condition on the bubble surface requires that it always be composed of the same fluid particles [Lamb 1932, p. 7], the curves of centroid and centerline position reflect the difference in the axial trajectory of actual fluid particles when the bubble is present. The centroid velocity curve shows the dramatic acceleration of the bubble and extends to a point which falls off the scale of the figure.

No exact expression has been found for the growth of the aspect ratio a/b for the experimental bubbles, but a close upper bound is given by the deformation of an initially spheroidal surface, imagined in the fluid, convecting with its axis along the centerline of the stagnation flow.

An ideal stagnation flow, along the z axis, into the origin of a Cartesian coordinate system, is described by the velocity potential [Prandtl and Tietjens 1934, p. 142; Batchelor 1967, p. 105]:

$$\phi = k \left(\frac{z^2 + y^2}{2} - z^2 \right). \quad (3.2)$$

It is clear that the z component of the velocity, $\nabla\phi$, anywhere in a plane at z parallel to the x - y plane is just the centerline velocity:

$$u = \frac{dz}{dt} = -2ks. \quad (3.3)$$

And a point initially at z_1 at time 0 moves toward the boundary such that its z coordinate at any time is:

$$z = z_1 e^{-2kt}. \quad (3.4)$$

and a point in the fluid approaches to $1/e$ of its initial distance from the boundary in a characteristic time $t_g = 1/2k$; and $2k = du/dz$; the constant velocity gradient of the flow. It follows that equally spaced planes in the fluid normal to the z axis remain equally spaced, but become closer as e^{-2kt} . Further, the velocity field is spheroidal so a closed surface in the fluid must enclose a constant volume as it deforms. Hence an initially spheroidal surface remains spheroidal, but becomes increasingly oblate. And it is easily shown that if the initial shape is a sphere:

$$\frac{a}{b} = e^{3kt}. \quad (3.5)$$

An estimate of the bubble aspect ratio, a/b_0 , at maximum radius is thus e^{3kt_R} , with k given by the velocity gradient at z_0 , determined from the free stream velocity U_∞ and either equation (2.1) or its representation in Figure 3.10. The values of e^{3kt_R} are listed in Table 3.1 for comparison with the measured aspect ratios a/b_0 . It is seen that the estimate is generally within 10% of the observed aspect ratio and, except for Bubble 2 which is too close to the boundary, the estimate is greater than the actual deformation. This might be expected since, near the bubble, the pressure gradient due to its pulsation is large compared to the pressure gradient of the stagnation flow for the experimental cases.

For the translational motion of a bubble, however, no simple

account can be given. While the magnitude of the total displacement of the bubble centroid is on the order of $2v_0 t_g$, actual motion is difficult to predict from inspection of the data. In particular, a priori determination of whether a bubble will accelerate into the stagnation region or bounce away from it is sought, and, to this end, a theory of the bubble motion is developed in the following chapter.

In closure a few remarks are in order. First it should be emphasized that the results of this research apply to stagnation flow into a rigid boundary. Gibson and Blake [1981] recently studied bubbles growing and collapsing near boundaries of various compliance and inertia and showed that these parameters have strong effect on the bubble motion and deformation. Some of the new modes of collapse they observed show strong resemblance to bubble geometries that develop in stagnation flow. For certain regimes of boundary inertia and stiffness, however, final bubble momentum and jetting are directed away from the boundary, and some of these boundaries are sufficiently "solid" to support stagnation flow. The behavior of a bubble in a stagnation flow into such a compliant boundary could clearly be radically different from what is observed here.

Next, it is implied in the discussion of Bubble 1 that bubbles collapsing near a boundary in the absence of flow produce only relatively thick slow jets. While this is true for bubbles close enough to jet on actual collapse, bubbles somewhat further from the boundary

can develop needle fine jets on rebound. This jetting mode was first seen for bubbles rebounding in a hydrostatic pressure gradient [Benjamin and Ellis 1966, Fig. 2], and excellent examples of its occurrence for bubbles rebounding near a wall are given by Lauterborn [1979]. While this is also observed in some of the no flow cases in the present study, unfortunately it occurs while the model is ringing from the impulse of the initial collapse shock and no estimate can be made of the force with which these jets strike the boundary, since it is apparently small enough to remain hidden by the model response.

Also the emphasis here on single bubble dynamics tends to oversimplify the nature of cavitation and the mechanisms of damage. The real complexities of flow induced cavitation are suggested by the pictures of cavitation shedding from the spark electrodes. For a proper appreciation of the role of single bubble studies in the context of actual cavitation and damage, the reader is referred to the book by Hammit [1980] which includes extensive references to the work of more than four hundred authors.

Finally, the study of bubble dynamics is by no means confined to the field of cavitation. A large and valuable literature on the subject is found in other areas as well. The classic papers of Walters and Davidson [1962, 1963], for example, were instrumental in forming the theoretical approach which is developed in Chapter IV to model the observed motion of a single spark bubble in the experimental stagnation flow.

CHAPTER IV THEORY OF THE BUBBLE MOTION

With the assumption that the flow is inviscid, incompressible, and irrotational, the motion of the fluid is given by a velocity potential ϕ where, if \vec{u} is the velocity at any point in the fluid:

$$\vec{u} = \nabla \phi \quad (4.1)$$

and ϕ is a solution of Laplace's equation:

$$\nabla^2 \phi = 0 \quad (4.2)$$

subject to the kinematical boundary condition that the normal velocity of the fluid on the boundary surfaces be equal to the normal velocity of the boundary at each point. On a free boundary such as the bubble surface there is the additional boundary condition that the pressure in the fluid be constant over the surface.

In the coordinate system of Figure 4.1 the flow is axisymmetric about the z axis. Taking the origin of the spherical polar coordinate system, (r, θ) , as translating with the bubble centroid, (z_c) , the solution of equation (4.2) is given by an expansion in spherical harmonics:

$$\phi = \sum_{n=0}^{\infty} (A_n r^n + B_n r^{-n-1}) P_n(\cos \theta) \quad (4.3)$$

Bubble No.	Figure	Capacitor (uF)	Standoff (mm)	U_m (cm/sec)	P_T (kPa)	Lifetime (uS)	t_R (uS)	U_0 (cm/sec)	P_0 (kPa)	R_0 (mm)	R_0/b_0	$3 \mu s_R$
1	3.1	0.02	2.8	0	103	630	265	0	103	2.80	2.00	-
2	3.2	0.02	2.7	590	102	665	290	147	101	2.55	3.10	1.27
3	3.3	0.04	4.9	1230	139	810	367	427	130	3.65	4.35	1.78
4	3.4	0.04	9.6	1840	287	460	221	1137	222	7.52	3.86	1.40
5	3.5	0.02	6.3	690	103	495	243	337	97	5.50	2.73	1.20
6	3.6	0.04	5.1	1220	141	690	326	449	131	3.90	3.85	1.65
7	3.7	0.02	10.0	1470	189	420	208	957	143	8.12	2.92	1.26
8	3.8	0.01	5.2	1220	141	430	213	472	130	4.12	2.52	1.38
9	3.9	0.02	5.0	1220	141	625	288	441	131	3.82	3.51	1.56

Table 3.1. Bubble and Flow Parameters

where the P_n 's are the Legendre polynomials and the coefficients A_n, B_n can be determined, in principle, from the boundary conditions and an initial condition on the bubble surface $r = R(\theta, t)$. If the equation for the bubble surface is expressed as:

$$F = r - R(\theta, t) = 0 \quad (4.4)$$

then the kinematical boundary condition [Lamb 1932, p. 7] is equivalent to:

$$\frac{DF}{Dt} = 0, \quad (4.5)$$

which also applies to the rigid boundary expressed in the form $F = 0$.

The pressure on the bubble surface may be found from the general Bernoulli equation referred to the moving coordinate system [Milne-Thompson 1968, p. 89] evaluated at $r = R$:

$$\left[\frac{p}{\rho} - \left(\frac{\partial \phi}{\partial t} - \vec{v} \cdot \nabla \phi + \frac{1}{2} (v_\theta)^2 + \Omega \cdot \frac{P_\infty(t)}{\rho} \right) \right]_{r=R} \quad (4.6)$$

where p is the pressure, ρ is the density, $\vec{v} = \frac{dz}{dt}$ is the velocity of the origin and the bubble centroid relative to the rigid boundary, Ω is the gravitational potential and $P_\infty(t)$ is the pressure at infinity. When (4.3) is substituted in (4.6) quadratic terms in the P_n 's appear from the v_θ terms of (4.6), but these may be re-expressed as sums in P_n [Whittaker & Watson 1927, p. 331] and the pressure on the bubble surface then has the form:

$$\left[\frac{p}{\rho} = \sum_{n=0}^{\infty} C_n P_n(\cos \theta) \right]_{r=R} \quad (4.7)$$

The boundary condition requiring constant pressures on the bubble surface is equivalent to requiring that the pressure be independent of θ and thus all the C_n 's for $n > 0$ must vanish identically. The equations:

$$\left[C_n = 0 \right]_{r=R}, \quad n > 0 \quad (4.8)$$

are a set of non-linear equations in the coefficients A_n, B_n .

The kinematical condition (4.5) is non-linear as well and also leaves the bubble shape $R(\theta, t)$ an unknown function to be determined as part of the solution. The analytical difficulties of such problems are well known and render a general solution intractable; either numerical or approximate methods must be used.

If the bubble is modeled as remaining spherical, considerable simplification results. The flow field may be constructed from a distribution of sources and sinks using the method of images, which automatically satisfies the boundary condition (4.5) on both the spherical bubble surface and the rigid plane boundary at $z = 0$. The coefficients A_n, B_n will then be explicit functions of $R(t)$ and $z_c(t)$, and although they will not, in general, satisfy the free boundary condition (4.8) for all $n > 0$, the condition $C_1 = 0$ can be satisfied and this will yield an equation of motion for the bubble centroid.

Consider the net axial thrust on the bubble, F_z , given by the z component of the pressure, $p \cos \theta$, integrated over the bubble surface, S :

$$F_z = \int_S p \cos \theta dS = 2\pi R^2 \int_0^\pi p \cos \theta \sin \theta d\theta. \quad (4.9)$$

Writing $\cos \theta = \mu = P_1(\mu)$, and substituting for p from equation (4.7):

$$F_z = 2\pi R^2 \int_{-1}^1 \left\{ \sum_{n=0}^{\infty} C_n P_n(\mu) \right\} P_1(\mu) d\mu \quad r=R \quad (4.10)$$

which, by virtue of the orthogonality of the Legendre polynomials, vanishes for all $n \neq 1$. For $n=1$:

$$F_z = \frac{4}{3} \pi \rho R^2 [C_1]_{r=R} = 0 \quad (4.11)$$

with vanishing C_1 , and F_z has physical dimensions of force. As will be shown, C_1 is, itself, a sum of terms which diminish as $(R/2a_c)^n$, and among the leading terms of (4.11) will be found the rate of change of the bubble's virtual momentum, the buoyant force repelling the bubble from the stagnation region, and the Bjerknes force attracting the bubble toward the stagnation point.

Thus the boundary condition that requires C_1 to vanish will yield an equation of dynamic equilibrium that may be regarded as a

statement of d'Alemberts principle. An observer translating with the bubble sees no acceleration and the rate of change of the virtual momentum appears as an inertial force.

Returning to equation (4.6), the pressure at infinity is taken as constant in this work but in any case p_∞ is not a function of θ and so does not contribute to the terms of C_1 . Furthermore, the acceleration of gravity is small compared to the pressure gradient encountered in the stagnation flow and, to good approximation, $\Omega \approx 0$.

C_1 is thus the $P_1(\cos \theta)$ coefficient of:

$$-\left[\frac{\partial \phi}{\partial t} - \vec{v}_c \cdot \nabla \phi + \frac{1}{2} (v\phi)^2 \right] = \sum_{n=0}^{\infty} C_n P_n(\cos \theta) \quad (4.12)$$

where:

$$\frac{\partial \phi}{\partial t} - \vec{v}_c \cdot \nabla \phi = \frac{\partial \phi}{\partial t} - v_c \cos \theta \frac{\partial \phi}{\partial r} + v_c \frac{\sin \theta}{r} \frac{\partial \phi}{\partial \theta} \quad (4.13)$$

and:

$$\frac{1}{2} (v\phi)^2 = \frac{1}{2} \left[\left(\frac{\partial \phi}{\partial r} \right)^2 + \frac{1}{r^2} \left(\frac{\partial \phi}{\partial \theta} \right)^2 \right]. \quad (4.14)$$

Anticipating the determination of the A_n 's and B_n 's, an approximation of equation (4.11) to $O(R/2a_c)^2$ can be obtained by retaining terms of (4.3) only through $n=2$, and:

$$\phi \approx [A_0 + B_0 r^{-1}] P_0 + [A_1 r + B_1 r^{-2}] P_1 + [A_2 r^2 + B_2 r^{-3}] P_2. \quad (4.15)$$

For reference the first few Legendre polynomials are:

$$P_0 = 1, P_1 = \cos \theta, P_2 = \frac{3}{2} \cos^2 \theta - \frac{1}{2}, P_3 = \frac{5}{2} \cos^3 \theta - \frac{3}{2} \cos \theta. \quad (4.16)$$

Taking the spatial derivatives of (4.15):

$$\frac{\partial \theta}{\partial r} = [-B_0 r^{-2}] P_0 + [A_1 - 2B_1 r^{-3}] P_1 + [2A_2 r - 3B_2 r^{-4}] P_2 \quad (4.17)$$

$$\frac{1}{r} \frac{\partial \theta}{\partial \theta} = -[A_1 + B_1 r^{-3}] \sin \theta - [A_2 r + B_2 r^{-4}] 3 \cos \theta \sin \theta. \quad (4.18)$$

When (4.17) and (4.18) are squared, only those products which are odd functions of $\cos \theta$ can contribute to the P_1 coefficient on the right hand side of (4.12); they are:

$$\begin{aligned} \text{From } \left(\frac{\partial \theta}{\partial r}\right)^2: & 2[-B_0 r^{-2}][A_1 - 2B_1 r^{-3}] P_0 P_1 \\ & + 2[A_1 - 2B_1 r^{-3}][2A_2 r - 3B_2 r^{-4}] P_1 P_2. \end{aligned} \quad (4.19)$$

$$\text{From } \frac{1}{r^2} \left(\frac{\partial \theta}{\partial \theta}\right)^2: 2[A_1 + B_1 r^{-3}][A_2 r + B_2 r^{-4}] 3 \sin^2 \theta \cos \theta. \quad (4.20)$$

And it is easily shown, without use of general formulae, that:

$$P_0 P_1 = P_1, P_1 P_2 = \frac{2}{5} P_1 + \frac{3}{5} P_3, \sin^2 \theta \cos \theta = \frac{2}{5} P_1 - \frac{2}{5} P_3. \quad (4.21)$$

So from (4.19) and (4.20) with (4.21), letting $r = R$, the contribution to C_1 from $\frac{1}{2}(\nabla \theta)^2$ on the bubble surface is:

$$2A_1 A_2 R - \frac{A_1 B_0}{R^2} - \frac{2}{5} \frac{A_2 B_1}{R^2} + \frac{2B_0 B_1}{R^5} + \frac{18}{5} \frac{B_2 B_3}{R^7}. \quad (4.22)$$

Also, from (4.17), (4.18), and (4.13) with (4.21) the contribution to C_1 from the convective term $-\vec{v} \cdot \nabla \theta$, at $r = R$ is:

$$\frac{v_c B_0}{R^2} - 2v_c \frac{A_2 R}{R} \quad (4.23)$$

and the contribution from $\left(\frac{\partial \theta}{\partial t}\right)_{r=R}$ is just:

$$\dot{B}_1 R + \frac{\dot{B}_1}{R} \quad (4.24)$$

where the dot indicates differentiation with respect to time. Adding the terms of (4.22), (4.23), and (4.24) the complete approximation of C_1 on the bubble surface is:

$$\begin{aligned} [C_1]_{r=R} = 0 = & \dot{B}_1 R + \frac{\dot{B}_1}{R} - 2v_c \frac{A_2 R}{R} + \frac{v_c B_0}{R^2} + 2A_1 A_2 R \\ & - \frac{A_1 B_0}{R^2} - \frac{2}{5} \frac{A_2 B_1}{R^2} + \frac{2B_0 B_1}{R^5} + \frac{18}{5} \frac{B_2 B_3}{R^7}. \end{aligned} \quad (4.25)$$

Construction of the flow field from sources and sinks begins with a source m at $z = l \gg z_c$ and its image in the $z = 0$ plane, a source m at $z = -l$. Then:

$$\phi = -\frac{m}{r_1} - \frac{m}{r_2} \quad (4.26)$$

where r_1 is the distance from the source at l to the field point, (r, θ), and r_2 is the distance from the source at $-l$ to the field point.

When $(1/r_1)$ and $(1/r_2)$ are each expanded in a series of Legendre polynomials, (4.26) becomes:

$$\phi = -\frac{m}{f-z_c} \sum_{n=0}^{\infty} \left(\frac{r}{f-z_c}\right)^n P_n(\cos \theta) - \frac{m}{f+z_c} \sum_{n=0}^{\infty} (-1)^n \left(\frac{r}{f+z_c}\right)^n P_n(\cos \theta). \quad (4.27)$$

Combining the two sums and evaluating the coefficients with $\frac{2m}{f^3} = k = \text{constant}$, terms higher than $n=2$ vanish to $O\left(\frac{1}{f}\right)^{n-2}$, and, disregarding the A_0 coefficient which does not appear in (4.25):

$$\phi = -2kz_c r P_1 - kr^2 P_2 \quad (4.28)$$

which is just the potential for the flow near a stagnation point [Prandtl and Tietjens 1934, p. 142; Batchelor 1967, p. 105] expressed in the coordinates (r, θ) with the origin at z_c . The condition $\frac{2m}{f^3} = k$ maintains the velocity at z_c independently of f . The stagnation flow thus gives the following contributions to the coefficients of (4.3):

$$\begin{aligned} \text{To } A_1: & -2kz_c \\ \text{To } A_2: & -k \end{aligned} \quad (4.29)$$

The remaining terms of the coefficients will contain terms in $\left(\frac{R}{z_c}\right)^n$ and to obtain (4.25) to $O\left(\frac{R}{z_c}\right)^2$ terms to $O\left(\frac{R}{z_c}\right)^3$ will have to be retained in B_0, B_2, A_2 because of the presence of $(-2kz_c)$ in A_1 . (A term in $2kz_c$ appears in B_1 , also.) The coefficients A_1, B_1

need be correct only to $O\left(\frac{R}{z_c}\right)^2$.

The translation of the spherical bubble, B, is represented by a doublet of strength $\frac{v R^3}{2}$ at the origin z_c , and the boundary condition at the $z=0$ plane is preserved with its image in $z=0$, an opposing doublet of equal strength at $-z_c$. Similarly, the pulsation of the bubble is represented with a source of strength $R^2 \dot{R}$ at z_c and its image at $-z_c$.

Finally the boundary conditions on the sphere B and its image A are maintained by a sequence of images at the respective inverse points in the two spheres, which, by symmetry also maintain the boundary condition on $z=0$.

Consider first the images of the stagnation flow in the two spheres. Each source (at f and $-f$) has an image in each sphere. In general, the image in a sphere of radius R of a source of strength m at a distance d from the center of the sphere is a source of strength $m \frac{R}{d}$ at the sphere's inverse point d' , and a line sink of constant density $\frac{m}{R}$ extending from d' to the center of the sphere, where $dd' = R^2$ [Milne Thompson 1968, p. 492]. With $f \gg z_c > R$ the inverse points are approximately at the centers of the spheres B, A and the images in each are two opposing doublets of slightly different strengths. The potential due to this system may conveniently be calculated by the use of Weisse's sphere theorem [Weisse

1944; Milne-Thompson 1968, p. 520], where if $\phi(r, \theta)$ is the velocity potential due to singularities outside the sphere of radius R , the potential due to their images in the sphere is:

$$\phi_1 = \frac{1}{R} \int_0^{R^2/r} x \frac{\partial \phi(x, \theta)}{\partial x} dx. \quad (4.30)$$

And taking $\phi(x, \theta) = -2kz_c x P_1 - kx^2 P_2$ from (4.28) the image of the stagnation flow in the sphere B is:

$$\phi_1 = \frac{-kz_c R^3}{2} P_1 - \frac{2kR^5}{3} P_2. \quad (4.31)$$

The first term is the net doublet strength at the center of B and represents a translation of B with velocity $2kz_c$ which is just equal and opposite to the velocity of the stagnation flow at z_c . The second term is the potential due to a quadrupole. A corresponding system of opposing doublet and quadrupole appear as an image at the center of sphere A . There follows a succession of images of these primary images at the respective inverse points in the two spheres. The complete sequence of inverse points may be described as follows.

Let $z_c = z_0 > z_1 > z_2 \dots z_m \dots$ be a sequence of points in B , and z'_m be the symmetrically corresponding points in A . Then if z_{m+1} is the inverse point in B of z'_m in A :

$$z_c - z_{m+1} = \frac{R^2}{z_c + z'_m}. \quad (4.32)$$

The solution for the potential due to the sequence of doublets is given by the well known problem of two spheres translating along their line of centers [Lamb 1932, p. 131; Milne-Thompson 1968, p. 525].

The image of a doublet of unit strength at, say, z'_m is an oppositely directed doublet of strength $\left(\frac{R}{z_c + z'_m}\right)^3$ at z_{m+1} . It is found that terms of the potential near B to $O\left(\frac{R}{z_c}\right)^3$ appear only in the A_1, B_1 coefficients; terms of higher coefficients are $O\left(\frac{R}{z_c}\right)^n, n > 3$, a result that can also be obtained from (4.30). The leading term in the

A_1 coefficient is $O\left(\frac{R}{z_c}\right)^3$ as is the second term in the B_1 coefficient. Since A_1 and B_1 are required only to $O\left(\frac{R}{z_c}\right)^2$ it is

sufficient to retain in the potential the contribution from the doublet at the center of B only. The same is true, of course, for the doublet representing the bubble's translation. Similarly, near B , the quadrupole potentials from the sphere A and all the images can be shown to be $O\left(\frac{R}{z_c}\right)^n, n > 3$. Thus the contributions to the

coefficients from the images of the stagnation flow are, from (4.31):

$$\begin{array}{ll} \text{To} & B_1: -kz_c R^3 \\ \text{To} & B_2: -\frac{2}{3}kR^5 \end{array} \quad (4.33)$$

and from the translational doublet $v_c \frac{R^3}{2}$.

$$\text{To } B_1: -\frac{v_c R^3}{2}. \quad (4.34)$$

Now the pulsation of the spheres is given first by the potential of the source $R^2 \dot{R}$ in B at z_c :

$$\phi = -\frac{R^2 \dot{R}}{r} \quad (4.35)$$

and of the image source $R^2 \dot{R}$ in A at $-z_c$:

$$\phi = -\frac{R^2 \dot{R}}{2z_c} \sum_{n=0}^{\infty} (-1)^n \left(\frac{r}{2z_c}\right)^n P_n(\cos \theta). \quad (4.36)$$

The system of images of these two sources begins with an image in B of the source at $-z_c$ in A, which is a source of strength

$R^2 \dot{R} \frac{R}{2z_c}$ at the inverse point $z_1 = \frac{R^2}{2z_c}$ and a line sink of equal

total strength extending from z_1 to the origin z_c . A corresponding source-line sink appear at z'_1 in A from the original source in B.

Now it has been shown [Hicks 1979] that the image of such a source-

line sink combination in a sphere is, itself, a source-line sink. If

for example, a source-line sink in A has its source at z'_m and its

line sink extends to z'_{m-1} then the image of this system in B is a

source at z_{m+1} , the inverse point of z'_m and a line sink extending

from z_{m+1} to z_m , the inverse point of z'_{m-1} . The strength of the source at z_{m+1} is $\frac{R}{z_c + z_m}$ times the strength of the source at z'_m . the associated line sink is of constant density and total strength equal to the source.

The potential from the image in B of the source at $-z_c$ can be found by again using (4.30). Taking $\phi(x, \theta)$ from (4.36) and dis-regarding the P_0 term:

$$\phi(x, \theta) = \frac{R^2 \dot{R}}{(2z_c)^2} x P_1 - \frac{R^2 \dot{R}}{(2z_c)^3} x^2 P_2. \quad (4.37)$$

And from (4.30)

$$\phi_1(x, \theta) = \frac{1}{2} \frac{R^2 \dot{R}}{(2z_c)^2} \frac{P_1}{r^2} - \frac{2}{3} \frac{R^2 \dot{R}}{(2z_c)^3} \frac{P_2}{r^3} \quad (4.38)$$

is the potential of the first source-line sink image in B. Clearly,

succeeding images in the two spheres will give rise to potentials near

B of $O\left(\frac{R}{2z_c}\right)^n$, $n > 3$ and the final contributions to A_n , B_n are

given by (4.35), (4.36) and (4.38):

$$\text{To } B_0: -R^2 \dot{R}$$

$$\text{To } B_1: \frac{1}{2} \frac{R^5 \dot{R}}{(2z_c)^2} \quad \text{To } A_1: \frac{R^2 \dot{R}}{(2z_c)^2} \quad (4.39)$$

$$\text{To } B_2: -\frac{2}{3} \frac{R^7 \dot{R}}{(2z_c)^3} \quad \text{To } A_2: -\frac{R^2 \dot{R}}{(2z_c)^3}.$$

Collecting the terms from (4.29), (4.33), (4.34), and (4.39):

$$\begin{aligned} B_0 &= -R^2 \dot{R} \\ B_1 &= \frac{1}{2} \frac{R^5 \dot{R}}{(2z_c)^2} - \frac{v_c R^3}{2} - k z_c R^3 \quad A_1 = \frac{R^2 \dot{R}}{(2z_c)^2} - 2k z_c \\ B_2 &= -\frac{2}{3} \frac{R^7 \dot{R}}{(2z_c)^3} - \frac{2}{3} k R^5 \quad A_2 = \frac{R^2 \dot{R}}{(2z_c)^3} - k \end{aligned} \quad (4.40)$$

Forming the terms of (4.25), and writing v_c for \dot{z}_c :

$$\begin{aligned} \dot{A}_1 R &= \frac{2R^2 \dot{R}^2}{(2z_c)^2} + \frac{R^3 \ddot{R}}{(2z_c)^2} - 2k v_c R + O\left(\frac{R}{2z_c}\right)^3 \\ \frac{\dot{B}_1}{R^2} &= \frac{5}{2} \frac{R^2 \dot{R}^2}{(2z_c)^2} + \frac{1}{2} \frac{R^3 \ddot{R}}{(2z_c)^2} - k v_c R - 3k z_c \dot{R} - \frac{1}{2} \frac{d}{dt}(v_c R^3) + O\left(\frac{R}{2z_c}\right)^3 \\ -2v_c A_2 R &= 2k v_c R + O\left(\frac{R}{2z_c}\right)^3 \\ \frac{v_c B_0}{R^2} &= -v_c \dot{R} \\ 2A_1 A_2 R &= 4k z_c^2 + O\left(\frac{R}{2z_c}\right)^5 \end{aligned}$$

$$-\frac{A_1 B_0}{R^2} = \frac{R^2 \dot{R}^2}{(2z_c)^2} - 2k z_c \dot{R} \quad (4.41)$$

$$-\frac{2}{5} \frac{A_2 B_1}{R^2} = -\frac{1}{5} k v_c R - \frac{2}{5} k^2 z_c R + O\left(\frac{R}{2z_c}\right)^3$$

$$\frac{2B_0 B_1}{R^5} = -\frac{R^2 \dot{R}}{(2z_c)^2} + v_c \dot{R} + 2k z_c \dot{R}$$

$$\frac{18}{5} \frac{B_1 B_2}{R^7} = \frac{6}{5} k v_c R + \frac{12}{5} k^2 z_c R + O\left(\frac{R}{2z_c}\right)^3.$$

Adding the terms of the expressions (4.41) gives the desired approximation of $[C]_{r=R}$ which, when substituted into (4.11) yields the equation of dynamic equilibrium for the bubble:

$$0 = \frac{4}{3} \pi \rho \left[-\frac{1}{2} \frac{d}{dt}(v_c R^3) + \frac{3}{2} \frac{R^4 (3\dot{R}^2 + R\ddot{R})}{(2z_c)^2} - 3k z_c R^2 \dot{R} + 6k^2 z_c R^3 \right]. \quad (4.42)$$

The first term is the rate of change of the bubble's virtual momentum relative to the rigid boundary. The second term is the same as the expression given by Hicks [1880] for the Bjerknes force. The third term is another inertial force, the rate of change of virtual momentum of a sphere whose volume is changing $\left(\frac{\partial}{\partial t} R^3\right)$ while translating with the velocity of the stagnation flow $(-2k z_c)$. The final term is the buoyant force from the pressure gradient of the stagnation flow. It is interesting to note that if the contribution to the potential from the

Images in B are omitted from the calculation, the last three terms are reduced by a factor of $\frac{2}{3}$. The final term would then be $(4k^2 z_c) \left(\frac{4}{3} \pi \rho R^3 \right)$ which is the buoyancy that would be experienced by a sphere in a uniform pressure gradient, $4k^2 z_c$ being $u \frac{du}{dz}$, the pressure gradient of the stagnation flow.

If, in addition, a further approximation is made: that the growth and collapse of the bubble proceed as though the bubble were in an infinite ideal liquid with no external boundaries or flow, then $R(t)$ is given by the Rayleigh theory and the terms in \dot{R} and \ddot{R} may be expressed as functions of R and $\frac{\Delta p}{\rho}$ where Δp is the difference between the pressure at infinity and the vapor pressure in the bubble, assumed constant.

The Rayleigh equation may be derived by substituting the

$$\text{potential } \phi = -\frac{R^2 \dot{R}}{r} \text{ in the Bernoulli equation } \frac{p}{\rho} = -\left(\frac{\partial \phi}{\partial t} + \frac{1}{2} (v\phi)^2 - \frac{p_\infty}{\rho} \right)$$

evaluated at the bubble surface $r = R$ where $p = p_v$, the vapor pressure. The result is known as the Rayleigh equation:

$$R \ddot{R} + \frac{3}{2} \dot{R}^2 = -\frac{p_\infty - p_v}{\rho} \quad (4.43)$$

Interestingly, Rayleigh [1917] did not express this result as a second order equation. He used a simple derivation based on energy conservation to obtain directly the form:

$$\dot{R}^2 = \frac{2}{3} \frac{\Delta p}{\rho} \left(\frac{R_0^3}{R^3} - 1 \right) \quad (4.44)$$

where R_0 is the maximum radius of the bubble. This equation may also be obtained by multiplying (4.43) by the integrating factor $R^2 \dot{R}$ and putting the result in the form $\frac{d}{dt} (R^3 \dot{R}^2) = -\frac{2}{3} \frac{\Delta p}{\rho} \frac{d}{dt} (R^3)$ which may be integrated directly to give (4.44). To obtain R as a function of time either (4.43) or (4.44) must be integrated numerically. The square root of (4.44) gives the bubble wall velocity, \dot{R} , as a function of wall radius, the sign of the radical taken as + or - according to whether the bubble is growing or collapsing.

Equation (4.44) may be used to express \dot{R} in the third term of (4.42) whose second term may also be expressed as $f(R)$ since $(3\dot{R}^2 + R\ddot{R}) = \frac{3}{2} \dot{R}^2 - \frac{\Delta p}{\rho}$ by virtue of (4.43). Then using (4.44) to express \dot{R}^2 , obtain:

$$(3\dot{R}^2 + R\ddot{R}) = \frac{\Delta p}{\rho} \left(\frac{R_0^3}{R^3} - 2 \right) \quad (4.45)$$

When these expressions are substituted into (4.42) and the first term is moved to the left hand side there results:

$$\frac{2}{3} \pi \rho \frac{d}{dt} (R^3 v_c) = \frac{4}{3} \pi \rho \left[\frac{2}{3} \frac{\Delta p}{\rho} \frac{R^4}{(2x_c)^2} \left(\frac{R_0^3}{R^3} - 2 \right) - 3k x_c R^2 \sqrt{\frac{2}{3} \frac{\Delta p}{\rho} \left(\frac{R_0^3}{R^3} - 1 \right) + 6k x_c R^3} \right]. \quad (4.46)$$

For comparison with the experimental data it is convenient to put (4.46) in nondimensional form with respect to the maximum bubble radius R_0 and t_R , the characteristic time to collapse from R_0 . As first shown by Besant [1859] who refers to the 1847 Cambridge Senate House problems, equation (4.44) may be recast as:

$$dt = \frac{dR}{\sqrt{\frac{2}{3} \frac{\Delta p}{\rho} \left(\frac{R_0^3}{R^3} - 1 \right)}} \quad (4.47)$$

which can be integrated over the whole range of R in terms of the

beta function, $B(m, n)$ to give t_R . Letting $\frac{R_0^3}{R^3} = x$,

$dR = -\frac{R_0}{3} x^{-2/3} dx$ and:

$$t_R = \frac{R_0}{3} \sqrt{\frac{2}{3} \frac{\Delta p}{\rho}} \int_0^1 x^{-2/3} \left(\frac{1}{x} - 1 \right)^{-1/2} dx. \quad (4.48)$$

Since $x^{-2/3} \left(\frac{1}{x} - 1 \right)^{-1/2} = x^{-1/6} x^{-1/2} \left(\frac{1}{x} - 1 \right)^{-1/2} = x^{-1/6} (1-x)^{-1/2}$

the integral may be written: $\int_0^1 x^{(5/6)-1} (1-x)^{(1/2)-1} dx = B\left(\frac{5}{6}, \frac{1}{2}\right) = \frac{\Gamma(\frac{5}{6}) \Gamma(\frac{1}{2})}{\Gamma(\frac{5}{6} + \frac{1}{2})}$ and when the gamma functions are evaluated, the result is:

$$t_R = 0.91468 R_0 \sqrt{\frac{\rho}{\Delta p}}. \quad (4.49)$$

Multiplying both sides of (4.46) by $\frac{3t_R^2}{4\pi\rho R_0^4}$ the equation is made

nondimensional. With a circumflex indicating the dimensionless quantity, and combining the numerical factors the equation of motion becomes:

$$\frac{d}{dt} \frac{(\hat{R}^3 \hat{v}_c)}{2} = \frac{0.314 (\hat{R} - 2\hat{R}_c)^4}{\hat{z}_c^2} - 2.24 \hat{k} \hat{z}_c (\hat{R} - \hat{R}_c)^{1/2} + 6 \hat{k} \hat{z}_c \hat{R}^3. \quad (4.50)$$

virtual momentum of the theoretically modeled bubble at any time, \hat{t} , is given by:

$$\text{virtual momentum} = \int_0^{\hat{t}} \hat{F}(\tau) d\tau, \quad (5.3)$$

which is labeled in the figures as: $\int \hat{F} d\hat{t}$, and is obtained by graphical integration of the curve \hat{F} for each of the bubbles, 7, 8, and 9.

The points plotted in the figures give two representations of the experimental bubble momentum. The bubble centroid velocity at each point in time is obtained from a curve like that of Figure 3.9c, derived by graphical differentiation of the centroid position. Multiplying the centroid velocity \hat{v}_c by the ellipsoidal bubble's virtual mass, $K\hat{R}^3$, (shown for Bubble 9 in Figure 3.9b) gives the experimental virtual momentum indicated by the squares in each figure. Also shown is the virtual momentum, $\frac{1}{2}\hat{R}^3\hat{v}_c$, which assumes the virtual mass of a sphere: $\frac{1}{2}\hat{R}^3$, and is represented with circles in Figures 5.1, 5.2, and 5.3. Note that force and momentum toward the rigid boundary are above the abscissa in each figure, but because the boundary is the z origin, the upward ordinate carries the negative sign.

It is interesting that Bubble 7, Figure 5.1, which bounces from the stagnation zone, and especially Bubble 8, Figure 5.2, which is the constant velocity case, are both better represented by the theory when considered as spheres rather than as ellipsoids. From

CHAPTER V BUBBLE MOMENTUM

The terms of equation (4.50) represent the apparent forces acting on the bubble in non dimensional form. Writing the equation as:

$$\hat{F} = \hat{F}_1 + \hat{F}_2 + \hat{F}_3; \quad (5.1)$$

where:

$$\hat{F} = \frac{d}{dt} \frac{\hat{R}^3 \hat{v}_c}{2}, \quad \hat{F}_1 = \frac{-314(\hat{R} - 2\hat{R}_0)}{z_c^2} \quad (5.2)$$

$$\hat{F}_2 = -2.24 \hat{k} \hat{z}_c (\hat{R} - \hat{R}_0)^{1/2}, \quad \hat{F}_3 = 6 \hat{k} \hat{z}_c \hat{R}^3;$$

\hat{F} is the total apparent force, or rate of change of the bubble's virtual momentum, relative to the rigid boundary. \hat{F}_1 is the net attractive Bjerknes force, \hat{F}_3 the buoyant force, and \hat{F}_2 is the rate of change of virtual momentum associated with the volume change of the bubble in the local velocity field of the stagnation flow. For Bubbles 7, 8, and 9 the terms \hat{F}_1 , \hat{F}_2 , and \hat{F}_3 are evaluated throughout the time interval $0 < \hat{t} < 2$, and are shown plotted with their sum, \hat{F} , in Figures 5.1, 5.2, and 5.3. To evaluate the terms, $\hat{z}_c(\hat{t})$ is taken from the observed centroid position of the experimental bubble. The non dimensionalizing factors, R_0 and t_R , are the experimental values as well, but $\hat{R}(\hat{t})$ is taken as given by the numerical integration of the Rayleigh equation, (4.43). The total

Figure 5.3, however, it is clear that Bubble 9's virtual momentum, $\int \hat{F} d\hat{t}$, as given by the theory closely follows (in form if not quite in magnitude) the experimental points for the ellipsoidal case. This difference may be due to the fact that the centroid of Bubble 9 begins to accelerate sharply with respect to the local stagnation flow velocity at about $\hat{t} = 1$. In contrast, Bubble 8, and Bubble 7 until very near its collapse, translate and deform more in accord with the local stagnation flow in the interval $1 < \hat{t} < 2$. This variation in behavior relative to the local velocity field is also evident from comparison of the curves \hat{F} and \hat{F}_2 in each of the Figures 5.1 - 5.3. The inertial force \hat{F}_2 reflects convection of the bubble with the stagnation flow, and Figures 5.1 and 5.2 show that the total force \hat{F} closely follows \hat{F}_2 for Bubbles 7 and 8, where the forces \hat{F}_1 and \hat{F}_3 remain symmetrically opposed. For Bubble 7 the Bjerknes force, \hat{F}_1 , is relatively insignificant and the buoyant force, \hat{F}_3 , effects a shift in \hat{F} , relative to \hat{F}_2 , but \hat{F} still has the form of \hat{F}_2 . For Bubble 8 the forces \hat{F}_1 and \hat{F}_3 are largely in balance throughout the history, so \hat{F} and \hat{F}_2 are close in magnitude as well as form in the interval around $\hat{t} = 1$. For Bubble 9, however, Figure 5.3 shows that the strong contribution of \hat{F}_1 , in skewed imbalance with \hat{F}_3 , results in marked deviation of \hat{F} from \hat{F}_2 . This, in turn, causes $\int \hat{F} d\hat{t}$ to peak later in the history and to follow more closely the form of the ellipsoidal momentum $K \hat{R}^3 \hat{v}_c$.

This comparison of the virtual bubble momentum given by the simplified theory with that given by the data suggests that the effective virtual mass of the bubble depends on its deformation relative to the flow in which it is imbedded. This notion is consistent with the concept of virtual mass given by Darwin [1953] which is also discussed by Milne-Thompson [1968, p. 244, p. 491]. Darwin considered the case of a body translating in a fluid at rest and showed that the body's virtual mass is associated with the net displacements of fluid particles, in a plane normal to the body's motion, caused by passage of the body across the plane. While Darwin's theory does not treat motion through a straining flow such as the stagnation flow, if it remains true that virtual mass is associated with the net relative displacement of actual fluid particles, then the virtual mass of an initial sphere, radius R , which deforms with the flow may well remain constant. If the deformed sphere acquires a velocity great in comparison to the local velocity, however, its shape will certainly alter its virtual mass. In either case the virtual momentum is associated with the momentum of fluid entrained with the motion of the body, and is the Kelvin impulse of the motion. This is not necessarily the total momentum of the fluid [Theodoresen 1941; Darwin 1953] which depends also on the specification of the outer boundaries where an additional impulse may be required to preserve the required motion.

Considering the degree of approximation adopted in the theory of Chapter IV, the theoretical and experimental momenta for all the bubbles are in reasonable agreement. For Bubble 8, the fit with the data for the spherical case is remarkable, though the predicted final momentum is slightly positive compared to the zero value observed. The somewhat more positive final momentum predicted for all the bubbles is most exaggerated for Bubble 7, and this may be due in part to the greater standoff distance of this bubble which puts it in a region where the flow is a poorer approximation of the ideal stagnation flow. It may also be due to the Kelvin impulse manifesting as vorticity before collapse is complete, in which case the experimental points underestimate its magnitude away from the boundary. This possibility is suggested by reference to the cine pictures of the collapse of the similar bubble, No. 4, Figure 3.4, where the development of the top portion of the bubble into the vortex ring (seen on rebound) is indicated well before collapse and the water actually appears to be multiply connected in the two frames proceeding the main collapse shock. Perhaps most surprising, though, is the agreement between the final theoretical and experimental momenta for Bubble 9. Because it is in close proximity to the boundary it might be expected that the forces omitted from the theory (which depend on $(1/z_c)^3$, $n \geq 3$) would be of increasing importance, but it is not immediately clear whether their inclusion would improve or degrade the fit with the data.

Bubble 9 collapses on the boundary and it is interesting to compare its momentum toward the boundary at $\hat{t} = 2$ with an estimate of the jet momentum. Like the jet from Bubble 3, the jet from Bubble 9 is estimated to have a velocity ~ 5000 m/sec. If the diameter of the jet is taken as 1/4 mm (the approximate diameter of pits found on the model) and its length is taken as the vertical extent of the bubble, ~ 1 mm, then the volume of the jet is $\sim 5 \times 10^{-5} \text{ cm}^3$ and its mass is $\sim 5 \times 10^{-5}$ gm. Actually the jet is probably at least a factor of 2 thinner than the pit diameter but it is also probably longer than 1 mm, and estimating the jet mass to be in the range of, say, $10^{-5} - 5 \times 10^{-5}$ gm, its momentum would be in the range of 5 - 25 gm-cm/sec. From Figure 5.3 the dimensionless virtual momentum of the bubble at $\hat{t} = 2$ is about 0.05 - 0.10, depending on the interpretation of virtual mass. Multiplying by $\frac{4}{3} \pi \rho R_0^3 \times R_0 / \hat{t}$ restores the momentum to dimensional form and the result is $\sim 10 - 20$ gm-cm/sec. While the estimates are somewhat speculative, it appears that the jet carries a substantial fraction of the fluid's translational Kelvin impulse.

Whether a bubble finally accelerates into the stagnation zone or is ultimately repelled from it is clearly dependent on the magnitude of the Bjerknes force, \hat{F}_1 . It is seen from the figure that \hat{F}_1 is initially directed away from the boundary, which accounts for the brief period of deceleration seen in the data for Bubbles 8 and 9, and

that in the final period of collapse \hat{F}_1 is again directed away from the boundary. But for the majority of the history, \hat{F}_1 is an attractive force and the net impulse from \hat{F}_1 is always directed toward the boundary. The relative magnitude of \hat{F}_1 required to accelerate the bubble into the stagnation region is suggested by the curves of Bubble 8, the transition case, in Figure 5.2 where, as already pointed out, \hat{F}_1 and \hat{F}_3 are approximately in balance. In particular, they are approximately equal at $\hat{t} = 1$, $\hat{R} = 1$, where $\hat{F}_2 = 0$. This suggests the criterion:

$$\left| \frac{\hat{F}_1}{\hat{F}_3} \right|_{\hat{R}=1} > 1. \quad (5.4)$$

for acceleration of the bubble toward the boundary. From equations (5.2) this dimensionless force ratio is:

$$\left| \frac{\hat{F}_1}{\hat{F}_3} \right|_{\hat{R}=1} = \left| \frac{z_c^2}{6 \hat{k}^2 \hat{z}_c \hat{R}^3} \right|_{\hat{R}=1} = \frac{0.523}{\hat{k}^2 \hat{z}_c^3} \Big|_{\hat{R}=1} = N_B. \quad (5.5)$$

Now \hat{z}_c at $\hat{R} = 1$ is z_0/R_0 ; also $\hat{k} = 1/2t_g$, where t_g is the time constant for the stagnation flow, and $\hat{k} = t_g/2t_g$. Substituting these values for \hat{z}_c and \hat{k} into equation (5.5) there results:

$$N_B = .209 \frac{t_g^2 R_0^3}{z_0^3} = .209 \frac{(R_0/t_g)^2 R_0}{(z_0/t_g)^2 z_0}. \quad (5.6)$$

But from equation (4.49):

$$\left(\frac{R_0}{t_g} \right)^2 = \frac{1}{(.915)^2} \frac{\Delta p}{\rho} = \frac{1}{(.915)^2} \frac{p_0}{\rho} \quad (5.7)$$

where $\Delta p = p_0$, the local pressure at z_0 , if the vapor pressure in the bubble is taken as zero. And from equation (3.3):

$$\left(\frac{z_0}{t_g} \right)^2 = (2kz_0)^2 = u_0^2 \quad (5.8)$$

where u_0 is the local stagnation flow velocity. Also $.209/(.915)^2 = 1/4$ when the exact numerical values are used. Substituting (5.7) and (5.8) into (5.6):

$$N_B = \frac{1}{8} \frac{p_0}{\rho} \frac{R_0}{z_0^2} \quad (5.9)$$

and since $\frac{1}{2} \rho u_0^2 = p_T - p_0$, where p_T is the total pressure at the stagnation point:

$$N_B = \frac{1}{8} \frac{p_0}{p_T - p_0} \frac{R_0}{z_0} = \frac{|\text{Bernoulli force}|}{|\text{Buoyant force}|} \Big|_{R=R_0} \quad (5.10)$$

And the three modes of bubble behavior on collapse are given by:

- A. Bubble accelerates into stagnation zone: $N_B > 1$.
- B. Bubble bounces away from stagnation zone: $N_B < 1$.
- C. Bubble velocity constant: $N_B \approx 1$.

The values of N_B for Bubbles 1-9 are computed from

equation (5.10) using the values of P_T , P_0 , s_0 , and R_0 given in Table 3.1, and the results are tabulated in Table 5.1 along with the observed behavior indicated by A, B, or C.

Table 5.1. Dimensionless Force Ratio

Bubble	N_B	Behavior
1	∞	A
2	15.3	A
3	2.15	A
4	.22	B
5	1.00	C
6	1.62	A
7	.14	B
8	.90	C
9	1.50	A

In the use of N_B as an indicator of bubble behavior, certain caution is advised. First, as in the experimental examples, the denominator, $P_T - P_0$, can involve a small difference between large numbers, and if this is the case the pressures must be known with sufficient precision. In fact, comparison of \hat{F}_1/\hat{F}_3 measured from the curves for Bubbles 7, 8, and 9 with the corresponding values of N_B given in Table 5.1 shows the latter to be somewhat in error. Second, N_B only indicates the direction of final acceleration and is not, in itself, a criterion for whether a bubble will collapse on the

boundary. But if the relative magnitudes of R_0 , s_0 , and $u_0^2 R$ are considered, a reasonable judgment can be made. Finally, the translation value of $N_B = 1$ applies to situations like the experimental one where the bubble is born in the stagnation region and its final impulse results only from the action of \hat{F}_1 , \hat{F}_2 , and \hat{F}_3 during its lifetime. A bubble swept along the free boundary of a supercavitating flow, for example, may enter the stagnation region abruptly, and with substantial virtual momentum. It is hoped, however, that the work here may provide a basis for understanding such cases as well.



FIGURE 2.4 MODEL PRIOR TO ASSEMBLY

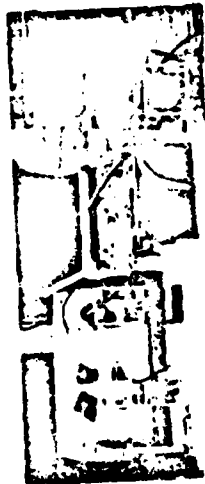


FIGURE 2.5 PULSE LOCKED RUBY LASER



FIGURE 2.6 HIGH SPEED CAMERA

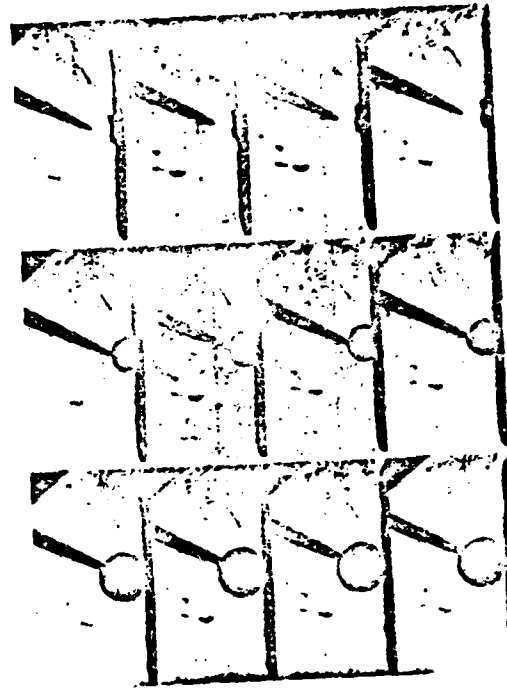
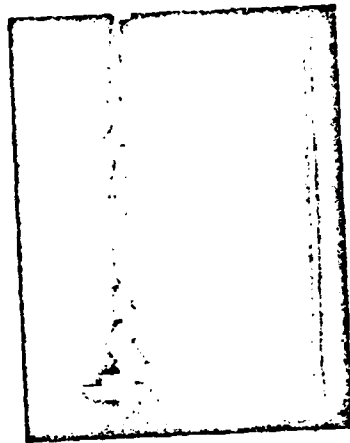


FIGURE 3.1 BUBBLE I OSCILLOGRAM AND CINE SEQUENCES

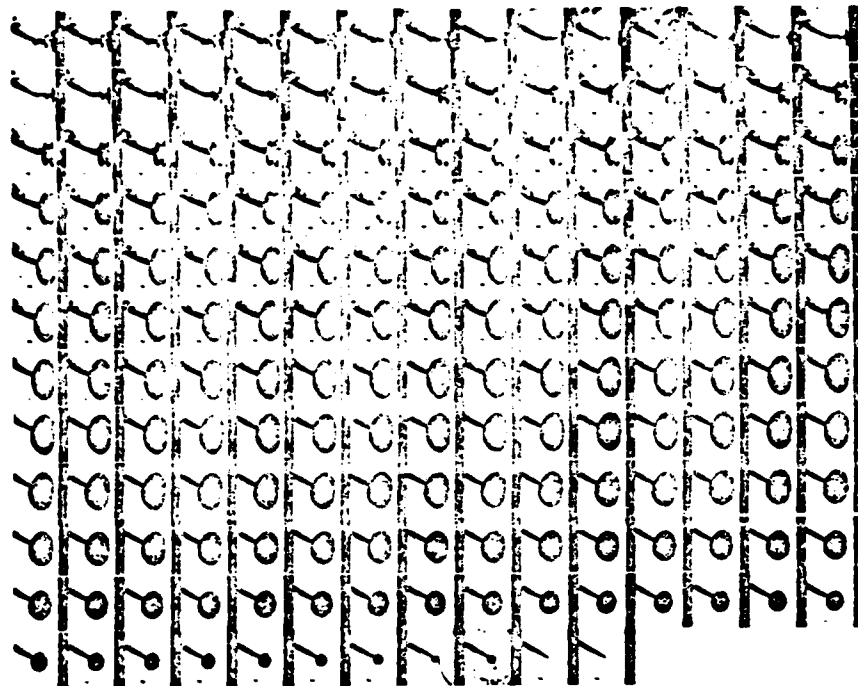


FIGURE 3.3 BUBBLE 3 COMPLETE CINE HISTORY

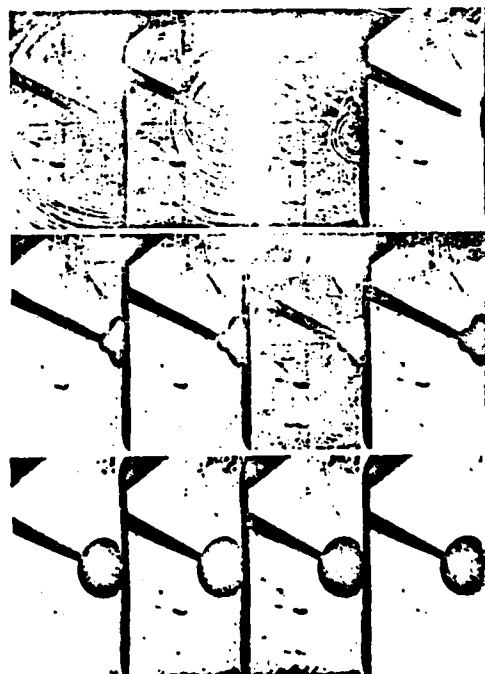
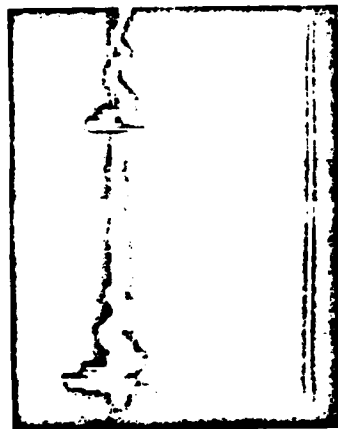


FIGURE 3.2 BUBBLE 2 OSCILLOGRAM AND CINE SEQUENCES

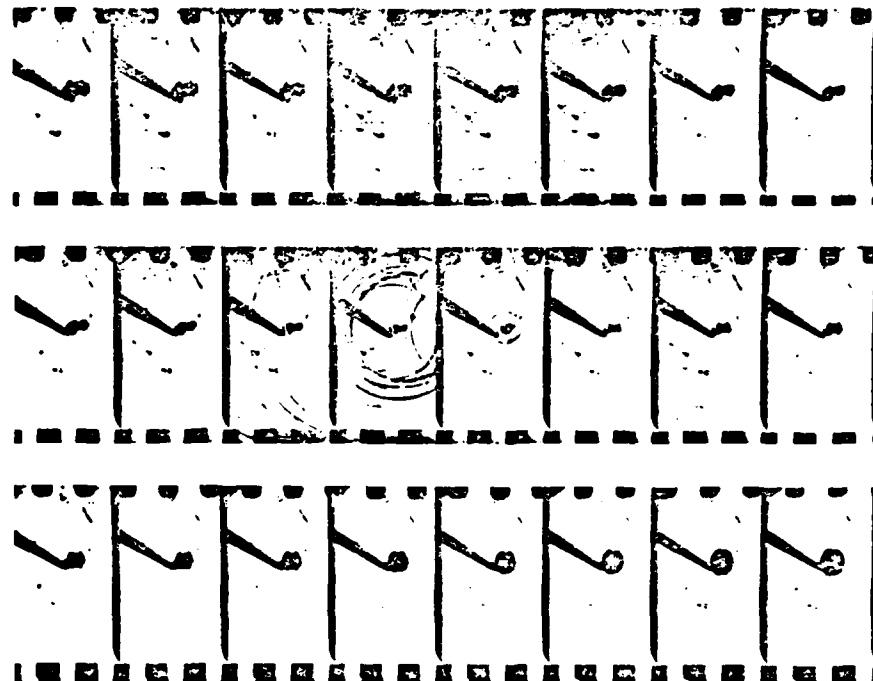


FIGURE 3.5 BUBBLE 5 COLLAPSE CINE SEQUENCE

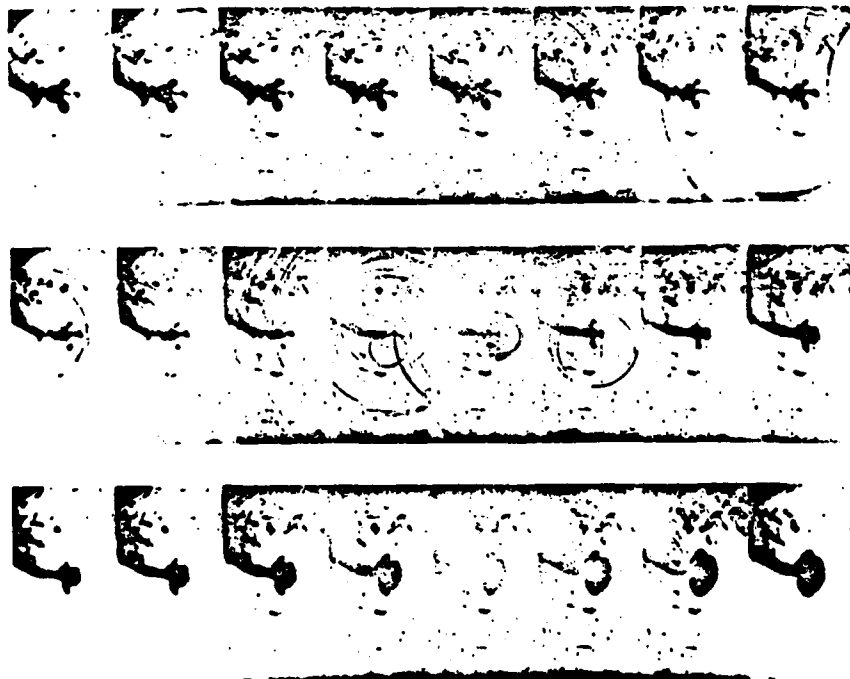


FIGURE 3.4 BUBBLE 4 COLLAPSE CINE SEQUENCE

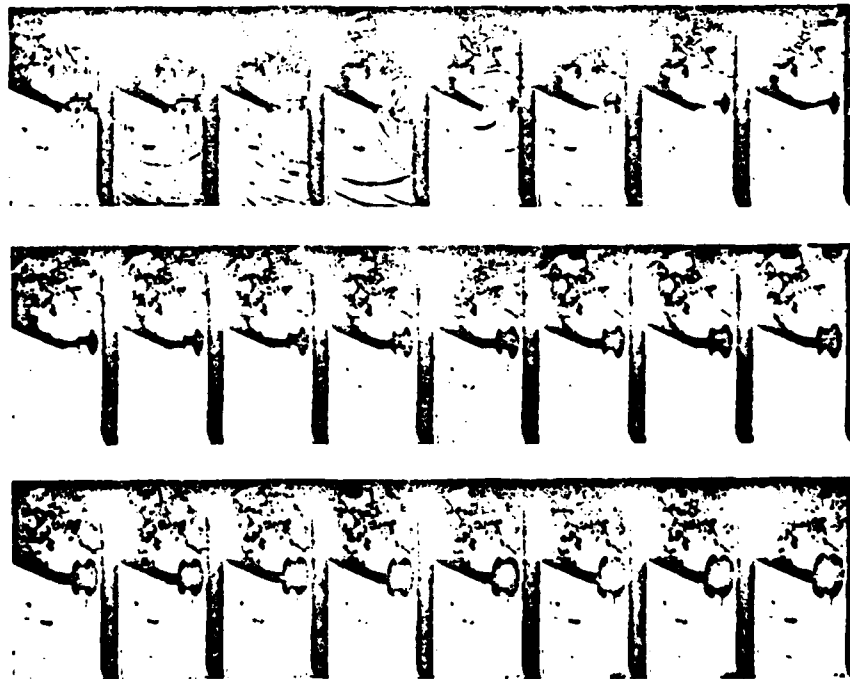


FIGURE 3.6 BUBBLE 6 COLLAPSE CINE SEQUENCE

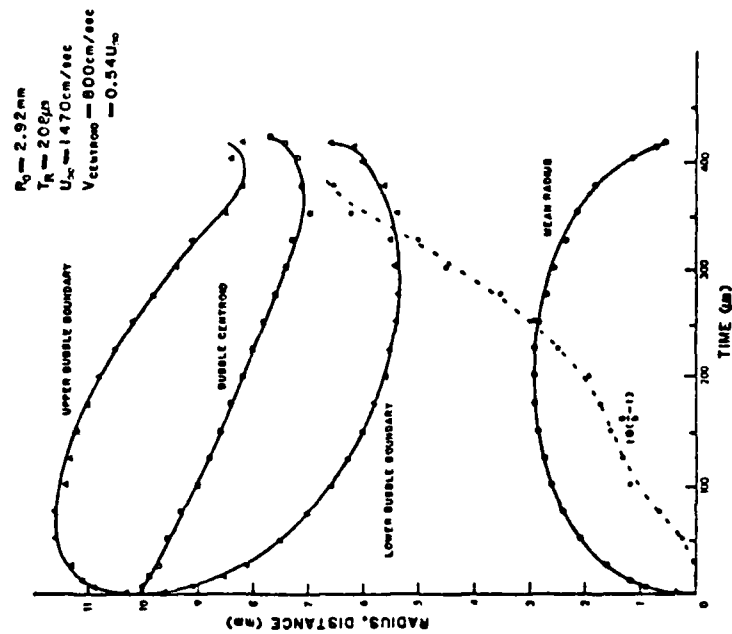
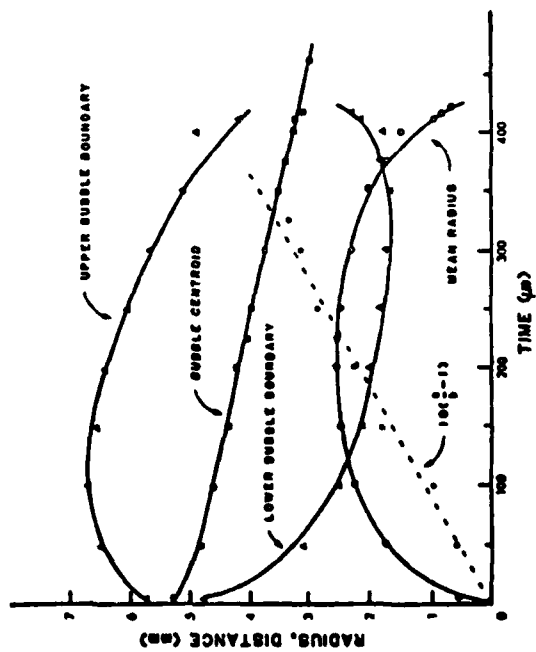


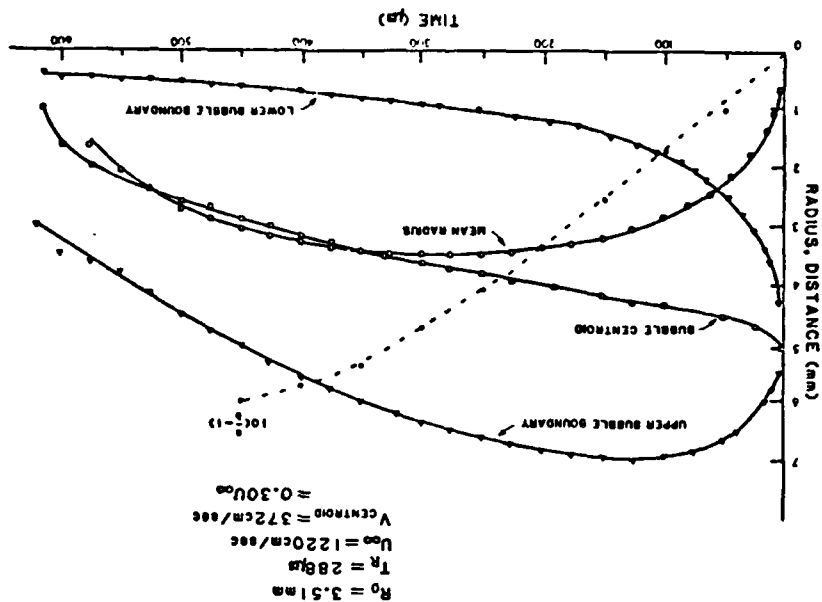
FIGURE 3.7 BUBBLE 7 MOTION HISTORY

FIGURE 3.8 BUBBLE 8 MOTION HISTORY



$R_0 = 2.52 \text{ mm}$
 $T_R = 213 \mu\text{s}$
 $U_{\infty} = 1220 \text{ cm/sec}$
 $V_{\text{CENTROID}} = 450 \text{ cm/sec}$
 $= 0.37 U_{\infty}$

FIGURE 3.9 BUBBLE 9 MOTION HISTORY



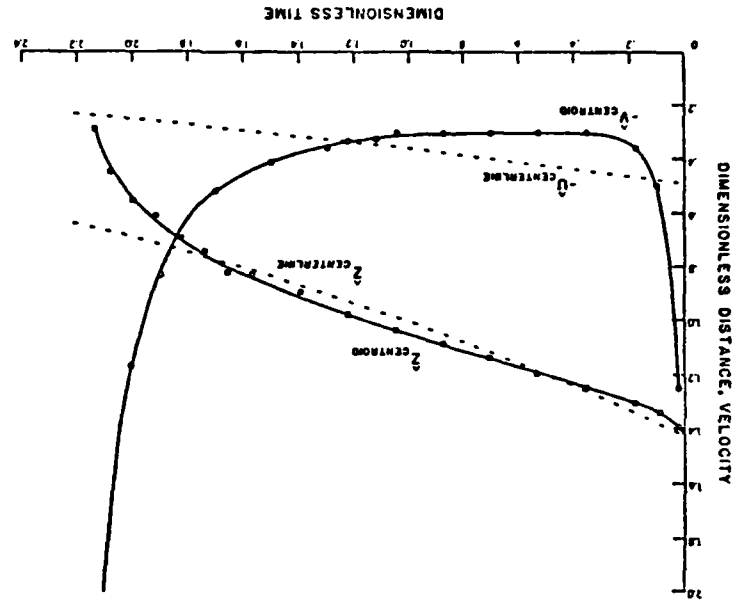
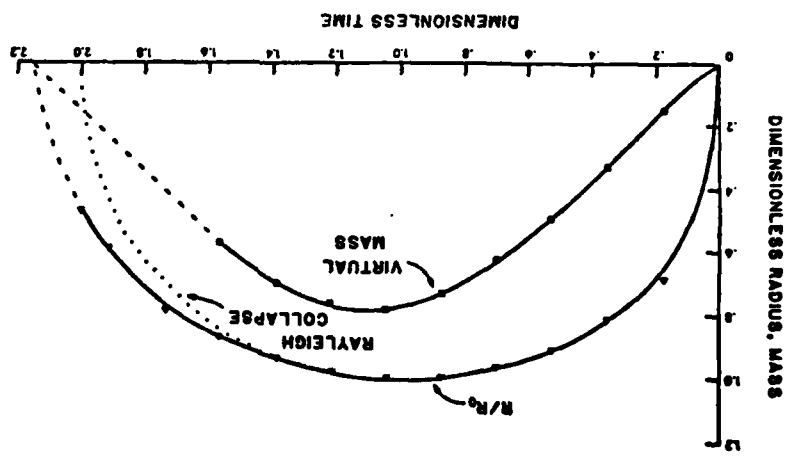


FIGURE 3.9b BUBBLE 9 DIMENSIONLESS RADIUS AND VIRTUAL MASS



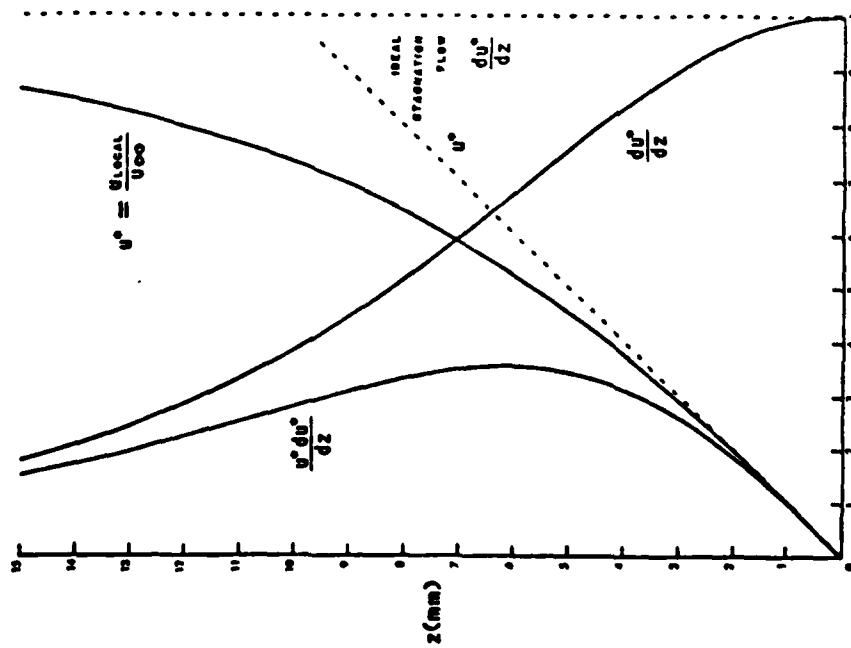


FIGURE 3.10 CENTERLINE VELOCITY

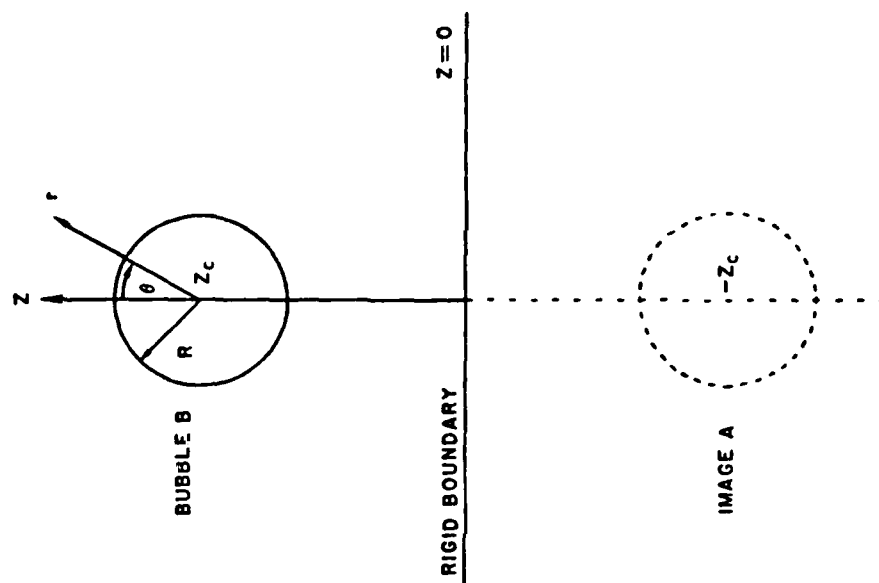


FIGURE 4.1 COORDINATE SYSTEM

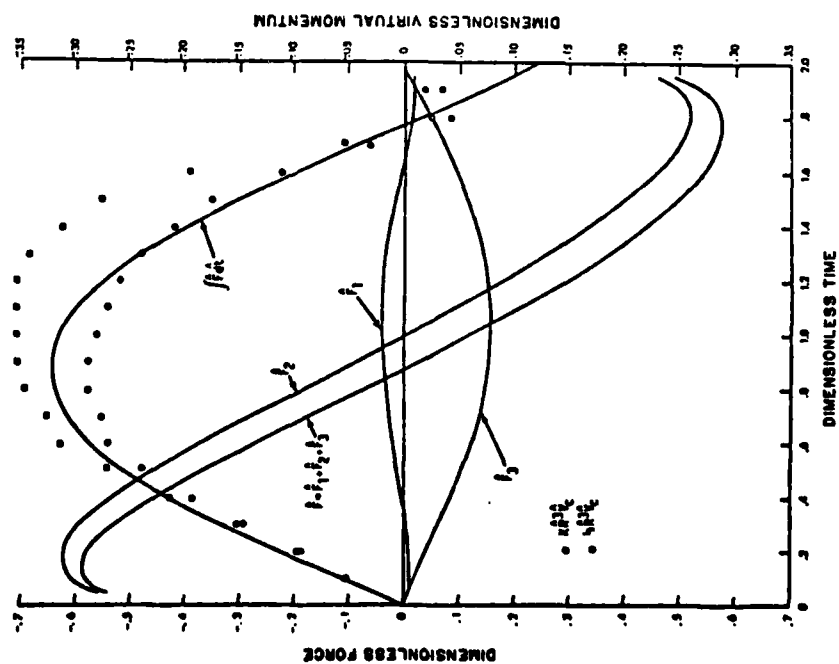


FIGURE 5.1 DIMENSIONLESS FORCE AND VIRTUAL MOMENTUM
BUBBLE 7

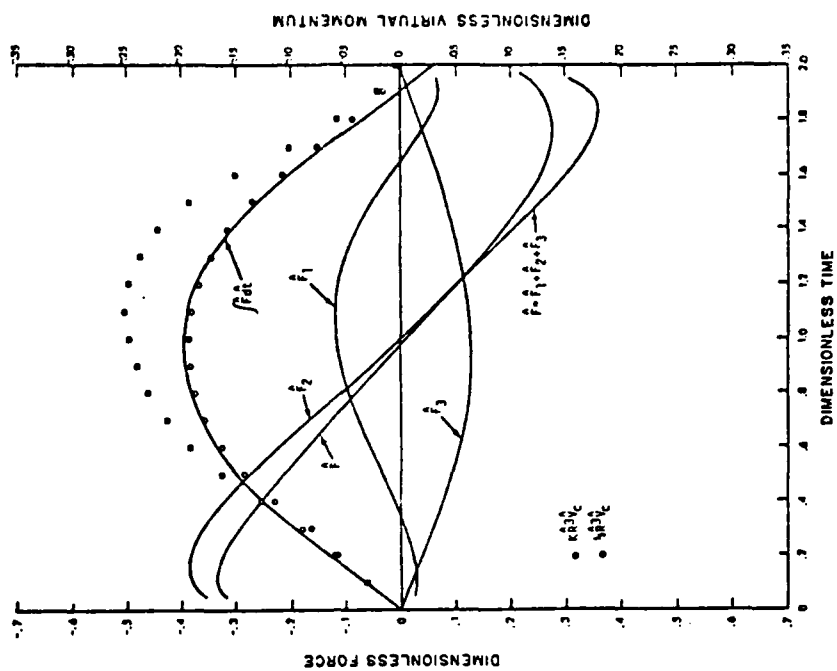


FIGURE 5.2 DIMENSIONLESS FORCE AND VIRTUAL MOMENTUM
BUBBLE 8

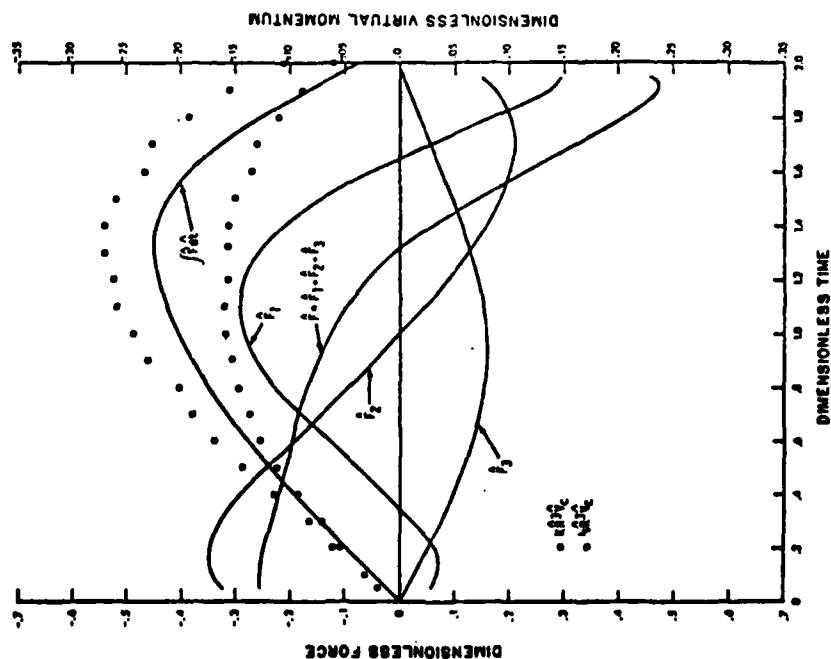


FIGURE 5.3 DIMENSIONLESS FORCE AND VIRTUAL MOMENTUM
BUBBLE 9

REFERENCES

- Batchelor, G. K. 1967, Fluid Dynamics, Cambridge University Press.
- Benjamin, T. B. and Ellis, A. T. 1966, "The collapse of cavitation bubbles and the pressures thereby produced against solid boundaries," Phil. Trans. Roy. Soc. London, A, Vol. 260, p. 221.
- Besant, W. H. 1859, A Treatise on Hydrostatics and Hydro-mechanics, §158, Cambridge.
- Birkhoff, G., MacDougall, D. P., Pugh, E. M. and Taylor, G. I. 1948, "Explosives with lined cavities," J. Appl. Phys., Vol. 19, p. 563.
- Chapman, R. B. 1970, "Nonspherical vapor bubble collapse," Doctoral Dissertation, California Institute of Technology.
- Chapman, R. B. and Plesset, M. S., 1972, "Nonlinear effects in the collapse of a nearly spherical cavity in a liquid," J. Basic Engng. Trans. Amer. Soc. Mech. Engrs., Vol. 94, p. 142.
- Cole, R. H., 1948, Underwater Explosions, Princeton University Press.
- Darwin, C., 1953, "Note on hydrodynamics," Proc. Camb. Phil. Soc., Vol. 49, p. 342.
- Ellis, A. T., 1966, "On jets and shock waves from cavitation," Proc. Sixth Symposium on Naval Hydrodynamics, p. 137.
- Office of Naval Research, Washington, D. C., R. D. Cooper and S. W. Doroff (eds.),
- Ellis, A. T. and Starrett, J. E., 1979, "Observations on bubble dynamics in jet flows and at high ambient pressure," Proc. 5th Int. Conf. on Erosion by Solid and Liquid Impact, p. 57-1, Cambridge.
- Euler, L., 1754, "Théorie plus complète des machines qui sont mises en mouvement par la réaction de l'eau," Mem. Acad. Roy. Science et Belles Lettres, Vol. 10, p. 227.

- Parsons, C. A. and Cook, S. S., 1919, "Investigations into the causes of corrosion or erosion of propellers," Engineering, Vol. 107, p. 515.
- Plesset, M. S., 1949, "The dynamics of cavitation bubbles," J. Appl. Mech., Vol. 16, p. 277.
- Plesset, M. S. and Chapman, R. B., 1971, "Collapse of an initially spherical vapor cavity in the neighborhood of a solid boundary," J. Fluid Mech., Vol. 47, p. 283.
- Plesset, M. S. and Ellis, A. T., 1955, "On the mechanism of cavitation damage," Trans. Amer. Soc. Mech. Engrs., Vol. 77, p. 1055.
- Plesset, M. S. and Mitchell, T. P., 1956, "On the stability of the spherical shape of a vapor cavity," Quart. Appl. Math., Vol. 13, p. 419.
- Prandtl, L. and Tietjens, O. G., 1934, Fundamentals of Hydro- and Aeromechanics, Dover Publications, Inc., N. Y.
- Ramsey, W., 1912, "Corrosion of bronze propeller blades," Engineering, May 24, 1912, p. 687.
- Rattray, M., 1951, "Perturbation effects in bubble dynamics," Doctoral Dissertation, California Institute of Technology.
- Rayleigh, Lord, 1917, "On the pressure developed in a liquid during the collapse of a spherical void," Phil. Mag., Vol. 34, p. 94.
- Reynolds, O., 1873, "The causes of racing of the engines of screw steamers investigated theoretically and by experiment," Trans. Inst. Naval Arch., Vol. 14, p. 56.
- Reynolds, O., 1874, "On the effect of immersion on screw propellers," Trans. Inst. Naval Arch., Vol. 15, p. 188.
- Reynolds, O., 1894, "Experiments showing the boiling of water in an open tube at ordinary temperatures," Papers on Mechanical and Physical Subjects, Vol. 2, p. 578, Cambridge University Press, 1902.
- Schlichting, H., 1968, Boundary Layer Theory, McGraw-Hill Book Co., N. Y.

- Callioe Callie, 1638, Two New Sciences, p. 25 of the Translation by Stillman Drake, Universality of Wisconsin Press, Madison, 1974.
- Cabon, D. C. and Blake, J. R., 1981, "The growth and collapse of bubbles near deformable surfaces," Appl. Sci. Res., Vol. 38, p. 215.
- Hamditt, F. G., 1980, Cavitation and Multiphase Flow Phenomena, McGraw-Hill Book Co., N. Y.
- Hicks, W. M., 1879, "On the problem of two pulsating spheres in a fluid," Proc. Camb. Phil. Soc., Vol. 3, p. 276.
- Hicks, W. M., 1880, "On the problem of two pulsating spheres in a fluid, Part II," Proc. Camb. Phil. Soc., Vol. 4, p. 29.
- Hatch, D. Y., 1972, "On the dynamics of nonspherical bubbles," J. Basic Engng., Trans. Amer. Soc. Mech. Engrs., Vol. 94, p. 655.
- Knaupp, R. T., 1955, "Recent investigations of the mechanics of cavitation and cavitation damage," Trans. Amer. Soc. Mech. Engrs., Vol. 77, p. 1045.
- Kornfeld, M. and Suworov, L., 1944, "On the destructive action of cavitation," J. Appl. Phys., Vol. 15, p. 495.
- Lamb, H., 1932, Hydrodynamics, 6th ed., Cambridge University Press.
- Lauterborn, W., 1979, "Liquid jets from cavitation bubble collapse," Proc. 5th Int. Conf. on Erosion by Solid and Liquid Impact, p. 58-1, Cambridge.
- Milne-Thompson, L. M., 1968, Theoretical Hydrodynamics, 5th ed., Macmillan Co., N. Y.
- Morgan, W. B. and Lichtman, J. Z., 1969, "Cavitation effects on marine devices," Cavitation State of Knowledge, p. 197 (see also "Discussions," p. 3), Robertson, J. M. and Wislicenus, G. F. (eds.), Amer. Soc. Mech. Engrs., N. Y.
- Naudé, C. F. and Ellis, A. T., 1961, "On the mechanism of cavitation damage by non-hemispherical cavities collapsing in contact with a solid boundary," Trans. Amer. Soc. Mech. Engrs., J. Basic Engng., Vol. 83, p. 648.

- Shima, A. and Nakajima, K., 1977, "The collapse of a non-hemispherical bubble attached to a solid wall," J. Fluid Mech., Vol. 80, Part 2, p. 369.
- Silberrad, D., 1912, "Propeller erosion," Engineering, Jan. 12, 1912, p. 33.
- Taylor, G. I., 1943, "The motion and shape of the hollow produced by an explosion in a liquid," The Scientific Papers of G. I. Taylor, Vol. III, p. 337, Batchelor, G. K. (ed.), Cambridge University Press, 1963.
- Theodoresen, T., 1941, "Impulse and momentum in an infinite fluid," Theodore von Karman Anniversary Volume, 1941, p. 49, California Institute of Technology.
- Ting, Y. R., 1971, "Cavitation dynamics and flow fields in dilute polymer solutions," Doctoral Dissertation, University of California, San Diego.
- Truesdell, C., 1954, "Rational Fluid Mechanics, 1687-1765," Editors Introduction to L. Euleri Opera Omnia II, Vol. 12, Lucanæ.
- Volnov, O. V. and Volnov, V. V., 1975, "Numerical method of calculating nonstationary motions of an ideal incompressible fluid with free surfaces," Sov. Phys. Dokl., Vol. 20, No. 3, p. 179.
- Volnov, O. V. and Volnov, V. V., 1976, "On the process of collapse of a cavitation bubble near a wall and the formation of a cumulative jet," Sov. Phys. Dokl., Vol. 21, No. 3, p. 133.
- Walsh, J. M., Shreffler, R. G. and Willig, F. J., 1953, "Limiting conditions for jet formation in high velocity collisions," J. Appl. Phys., Vol. 24, p. 349.
- Walkers, J. K. and Davidson, J. F., 1962, "The initial motion of a gas bubble formed in an inviscid liquid, Part 1. The two-dimensional bubble," J. Fluid Mech., Vol. 12, p. 408.
- Walkers, J. K. and Davidson, J. F., 1963, "The initial motion of a gas bubble formed in an inviscid liquid, Part 2. The three-dimensional bubble and the toroidal bubble," J. Fluid Mech., Vol. 17, p. 321.

- Weiss, P., 1944, "On hydrodynamical images, arbitrary irrotational flow disturbed by a sphere," Proc. Camb. Phil. Soc., Vol. 40, p. 259.
- Whittaker, E. T. and Watson, G. N., 1927, A Course of Modern Analysis, 4th ed. Cambridge University Press.